Resolved Turbulence Characteristics in Large-Eddy Simulations Nested within Mesoscale Simulations Using the Weather Research and Forecasting Model

JEFF MIROCHA

Lawrence Livermore National Laboratory, Livermore, California

BRANKO KOSOVIĆ

National Center for Atmospheric Research, Boulder, Colorado

GOKHAN KIRKIL*

Lawrence Livermore National Laboratory, Livermore, California

(Manuscript received 15 February 2013, in final form 24 September 2013)

ABSTRACT

One-way concurrent nesting within the Weather Research and Forecasting Model (WRF) is examined for conducting large-eddy simulations (LES) nested within mesoscale simulations. Wind speed, spectra, and resolved turbulent stresses and turbulence kinetic energy from the nested LES are compared with data from nonnested simulations using periodic lateral boundary conditions. Six different subfilter-scale (SFS) stress models are evaluated using two different nesting strategies under geostrophically forced flow over both flat and hilly terrain. Neutral and weakly convective conditions are examined. For neutral flow over flat terrain, turbulence appears on the nested LES domains only when using the two dynamic SFS stress models. The addition of small hills and valleys (wavelengths of 2.4 km and maximum slopes of $\pm 10°$) yields small improvements, with all six models producing some turbulence on nested domains. Weak convection (surface heat fluxes of 10 $W m^{-2}$) further accelerates the development of turbulence on all nested domains. However, considerable differences in key parameters are observed between the nested LES domains and their nonnested counterparts. Nesting of a finer LES within a coarser LES provides superior results to using only one nested LES domain. Adding temperature and velocity perturbations near the inlet planes of nested domains shows promise as an easy-to-implement method to accelerate turbulence generation and improve its accuracy on nested domains.

1. Introduction

Atmospheric models supporting local mesh refinement are frequently used to downscale coarse-resolution simulations. Downscaling within the mesoscale realm has been shown to produce more accurate and higher-fidelity results (e.g., Caldwell et al. 2009; Liu et al. 2011), by incorporating higher-resolution land surface data and resolving smaller scales of atmospheric motion, the effects of which must otherwise be parameterized. Based on these successes, downscaling is increasingly being extended to resolutions permitting the large-eddy simulation (LES) approach, whereby the three-dimensional turbulence providing energy to the classical inertial subrange is explicitly resolved. Such an approach can potentially reduce errors from mesoscale planetary boundary layer (PBL) parameterizations, most of which are based on the assumption of boundary layer homogeneity over a grid cell, and therefore implicitly not designed for use at very high resolutions. High-resolution simulations involving heterogeneous terrain or forcing require LES,

* Current affiliation: Department of Energy Systems Engineering, Kadir Has University, Kadir Has Caddesi, Cibali, Istanbul, Turkey.

Corresponding author address: Jeff Mirocha, Atmospheric, Earth and Energy Division, Lawrence Livermore National Laboratory, P.O. Box 808, L-103, Livermore, CA 94551.
E-mail: mirocha2@llnl.gov

DOI: 10.1175/MWR-D-13-00064.1

which explicitly resolves the scales of motion responsible for most of the stress and turbulent kinetic energy (TKE). Such high-resolution simulations are essential for many applications, including for example, transport and dispersion, wind resource characterization, and wind turbine siting.

Atmospheric models such as the Weather Research and Forecasting Model (WRF; Skamarock et al. 2008) permit downscaling via grid nesting, wherein the lateral boundary conditions for a nested domain are provided by the bounding simulation. Nests can be implemented within one another to achieve stepwise reductions in mesh spacing, permitting both large scales of weather and finer mesoscale features to influence the LES nested within. This approach can potentially provide the LES with more realistic atmospheric forcing than is traditionally obtained via offline coupling between mesoscale and LES models (e.g., Zajaczkowski et al. 2011). Nesting within the same code also eliminates inconsistencies between the grid structures, physical process models, and numerical solution methods encountered when coupling different models. In addition to one-way nesting, for which the bounding domain receives no feedback from the nested domain, WRF also facilitates two-way nesting, whereby information from the nested domain influences the bounding simulation. While two-way nesting is needed when effects resolved on a finer resolution nest are required by the solution on the bounding domain, many ABL and microscale applications simply require downscaling, where accurate large-scale forcing is essential, and for which one-way nesting is sufficient. We focus on one-way nesting herein.

While mechanisms for downscaling from mesoscale to LES exist in WRF (and other models), the extant methodology is constrained by shortcomings of current parameterizations and approaches. Wyngaard (2004) details challenges to developing closure models for unresolved turbulence effects in the terra incognita, a range of scales between traditional mesoscale (greater than 1 km) and LES (order of 1 km or less). Mirocha et al. (2013) and Moeng et al. (2007) describe difficulties involved in nesting finely resolved LES within a coarser-resolution LES within WRF, for which adequate closure models exist, yet for which errors are introduced into the nested LES solution via the nesting procedure. Moeng et al. (2007) were able to recover reasonable LES performance in nested LES under moderately strong forcing, but only after modifying the subfilter turbulence model, and using nested domains of sufficient sizes. Mirocha et al. (2013) investigated neutral flow over flat terrain and showed large departures in mean wind speed, stress, and resolved TKE within the nested LES, relative to single-domain simulations conducted on identical meshes, but instead using periodic lateral boundary conditions. These errors gradually attenuated with distance within the nested domains, yet often remained large, even several kilometers (several hundred grid cells) downstream. Additional problems related to both mesh refinement (e.g., Vanella et al. 2008; Piomelli et al. 2006) and the instigation of turbulence at laminar inflow boundaries for LES (e.g., Keating et al. 2004) have been identified.

Despite these caveats, downscaling from mesoscale to LES is increasingly being employed in an attempt to improve the fidelity and realism of atmospheric simulations. Unfortunately, little information exists regarding conditions under which the approach is appropriate, and what the potential errors might be. This study extends the work of Mirocha et al. (2013) to the nesting of LES within mesoscale flows, for which the inflow contains essentially no resolved turbulence. Many practitioners of downscaling expect that turbulence will spontaneously develop within a short distance from the inflow boundaries to nested LES domains due to the reduced mesh spacing. We investigate the veracity of this assumption under three forcing scenarios: neutral and weakly convective flow over flat terrain, and neutral flow over hilly terrain. We evaluate six different subfilter-scale (SFS) stress modeling approaches, and two different nesting methodologies. We also examine the addition of perturbations to the potential temperature and velocity fields near the inflow boundaries of nested domains as a simple-to-implement method to improve turbulence generation and flow characteristics downstream. The goal of this study is to inform WRF users of current limitations, provide the best practices, and to elucidate fruitful areas for future research.

2. Methodology

This study examines the accuracy of low-order statistics obtained from LES nested within mesoscale simulations using WRF. The base simulation is neutral flow over flat terrain, using a roughness length of $z_0 = 0.1$ m, forced by a geostrophic wind, $U_g = 10\,\mathrm{m\,s^{-1}}$, constant in time and height, oriented in the x direction, with a Coriolis parameter of $f = 0.0001\,\mathrm{s^{-1}}$ ($\cong 45°$N). The Mellor–Yamada–Nakanishi–Niino (MYNN; Nakanishi and Niino 2004) PBL scheme is chosen for the mesoscale domain, as this scheme provided the best performance among five models in a recent validation study using similar forcing to that applied herein (Muñoz-Esparza et al. 2012). Periodic lateral boundary conditions are used for the mesoscale domain, permitting the flow to approach equilibration with the forcing. The mesoscale domain utilizes horizontal mesh spacing

of $\Delta x = \Delta y = 297$ m, where x and y denote horizontal directions. While this mesh spacing is finer than traditional mesoscale applications, it is typical of an intermediate nested domain between a mesoscale simulation and an LES in a multiply nested downscaling application. This resolution is sufficiently coarse (relative to the forcing) to prevent the development of a classical three-dimensional turbulence spectrum within the mesoscale domain; that spectrum can only develop within the finer mesh resolutions of the LES domains nested within.

The accuracies of turbulence parameters produced within the nested LES are evaluated by comparison with stand-alone (nonnested) LES. The stand-alone LES use computational meshes that are identical to those of the nested LES, and use the same large-scale forcing, but instead utilize periodic lateral boundary conditions directly, providing the stand-alone LES with essentially unlimited fetches upon which turbulence can develop to statistically steady behavior. Rather than evaluating the accuracies of the SFS stress models themselves (as done previously, see Mirocha et al. 2010; Kirkil et al. 2012), here we take the stand-alone solutions as the ''truth,'' for each SFS stress model, and examine the development of flow and turbulence characteristics within the nested LES domains relative to the stand-alone solutions.

Two LES domains are nested within the mesoscale domain, as depicted in Fig. 1. The larger nested domain is a coarse LES, using $\Delta x = \Delta y = 99$ m, while the smaller is a fine LES, with $\Delta x = \Delta y = 33$ m. As WRF does not currently support vertical mesh refinement for concurrent nesting, all simulations use a vertical mesh spacing of $\Delta z^1 \cong 8.25$ m, where z denotes the vertical direction, and superscript 1 denotes the first model grid cell above the surface. This grid spacing yields a grid aspect ratio of $\alpha = \Delta x/\Delta z \cong 4$ near the surface on the fine LES domains, the primary areas of focus. This value of α has been found to yield the closest agreement with the logarithmic similarity profile for the mean wind speed U for neutral flow over flat terrain, with $z_0 = 0.1$ m (see Mirocha et al. 2010; Kirkil et al. 2012). The vertical grid is stretched by 5% per Δz, up to the model top, $\cong$2525 m.

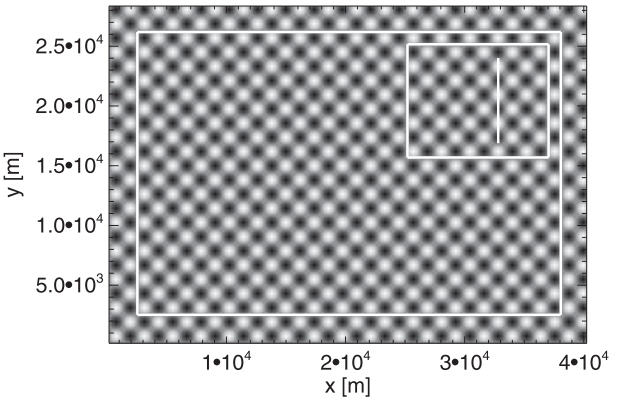

FIG. 1. Computational environment. Large and small white rectangles show coarse and fine nested LES domain locations, respectively, within the mesoscale domain. Background shows sinusoidal hills (light) and valleys (dark) used in undulating terrain simulations; otherwise, the terrain is flat. The thin white line shows P65, the location 65% of the distance across the fine LES domain, from left to right, from which various parameters are evaluated.

The heights of WRF's pressure-based vertical coordinate levels were specified from prescribed Δz values using the hypsometric equation (e.g., Holton 1992), and a surface pressure of 1×10^5 Pa. The resulting heights cannot be specified precisely in this manner; however, they vary by at most a few percent. A Rayleigh damping layer with a coefficient of $0.003\,\mathrm{s}^{-1}$ is applied to the upper 1 km of each domain. WRF imposes $w = \tau_{ij} = 0$ (w is the vertical velocity) at the model top. WRF's default fifth- and third-order horizontal and vertical advection schemes, respectively, are used. Physical and computational dimensions of simulations are provided in Table 1.

As the primary focus of this study is the development of resolved turbulence on nested LES domains under the challenging conditions of weak forcing, three scenarios are investigated: neutral flow over flat terrain, as described above; neutral flow over sinusoidal hills and valleys, with wavelengths of 2.4 km in each direction and maximum slopes of $\pm 10°$; and weakly convective flow over flat terrain, using a surface heat flux of $H_S = 10\,\mathrm{W\,m^{-2}}$. All simulation use the same values of U_g, f, and z_0. Three nesting strategies are employed, nesting coarse and fine LES within the mesoscale domains, and nesting the fine

TABLE 1. Physical and computational dimensions of simulation domains, where nx, ny, and nz are the number of grid points in the x, y, and z directions, respectively; Δx and Δz^1 are the horizontal and vertical grid spacings, with superscript 1 indicating the first grid point above the surface; $\alpha = \Delta x/\Delta z^1$ is the aspect ratio at the first grid cell above the surface; and L_x, L_y, and L_z are the domain dimensions. The CN, F1N, and F2N domains begin at $[i, j] = [9, 9], [85, 53]$, and $[229, 133]$ within the M and CN domains, respectively.

	nx	ny	nz	Δx (m)	Δz^1 (m)	α	L_x (m)	L_y (m)	L_z (m)
Mesoscale (M)	151	101	58	297	8.25	36	40 392	28 512	2525
Coarse LES (CN, CSA)	361	341		99		12	35 640	23 760	
Fine LES (F1N, F2N, FSA)	361	289		33		4	11 880	9504	

LES within the coarse nested LES. Finally, perturbations are added to the potential temperature and horizontal velocities near the inflow planes of nested LES domains as a technique to accelerate turbulence generation.

a. Modeling of subfilter-scale fluxes in LES

Here we briefly introduce the modeling of SFS fluxes, and provide further details in the appendix. The LES technique uses a low-pass filter,

$$\tilde{\varphi} = \int G(x_i, x_j')\varphi(x_j')\, dx_j', \tag{1}$$

to remove scales smaller than the filter width from the flow. Here G is the filter kernel, φ denotes model variables, $i, j = 1, 2, 3$, and x_i denotes spatial directions. The filter kernel G can denote either application of an explicit filter, or, as in WRF, implicit filtering arising from the discrete numerical solution procedure.

Application of Eq. (1) to the governing flow equations results in unclosed terms for the SFS momentum fluxes (or stresses),

$$\tau_{ij} = \widetilde{u_i u_j} - \tilde{u}_i \tilde{u}_j, \tag{2}$$

and scalar fluxes,

$$s_j = \widetilde{u_j q} - \tilde{u}_j \tilde{q}, \tag{3}$$

which must be modeled. Here, u_i denotes the velocity components, and q denotes a scalar.

We examine six different approaches to modeling the SFS stresses and fluxes. The simplest are two linear constant-coefficient eddy viscosity models. The Smagorinsky model (SMAG; Smagorinsky 1963; Lilly 1967) uses the strain rate, a length scale based upon the local grid spacing, and one coefficient. The TKE model, similarly based, also uses SFS TKE, obtained from an additional equation. The Nonlinear Backscatter and Anisotropy models (NBA1 and NBA2; Kosović 1997) include additional nonlinear terms consisting of products of the strain and rotation rate tensors. The NBA2 model incorporates SFS TKE from the TKE model's SFS TKE equation. As the NBA models only provide momentum fluxes, scalar fluxes are obtained from the SMAG (NBA1) or TKE (NBA2) models.

The above four SFS stress models are contained in the current WRF release (as of version 3). We also examine two dynamic models not in the current release. These models utilize explicit spatial filters to obtain spatially and temporally varying values of the coefficient used in the SMAG closure. The Lagrangian-Averaged Scale-Dependent (LASD; Bou-Zeid et al. 2005, 2008) model uses two spatial filters to extrapolate the value of the coefficient used for the SFS stresses from resolved stresses at two scales. The coefficients are stabilized by averaging along fluid pathlines. The Dynamic Reconstruction Model (DRM; Chow et al. 2005) uses a scale-invariant dynamic approach based on one level of filtering to obtain the coefficient. The scale-similarity term is obtained using explicit filtering and reconstruction, which provides variable orders of reconstruction. In this study we use the lowest order, level 0 (DRM0).

b. Surface boundary conditions

The surface stresses τ_{i3}^s, $i = 1, 2$, are obtained using Monin–Obukhov similarity, as

$$\tau_{i3}^s = -C_D U^1 u_i^1. \tag{4}$$

Here, U^1 and u_i^1 are the resolved wind speed and horizontal velocities, respectively, at their first computed height above the surface, and $C_D = \kappa^2\{\ln[(z^1 + z_0)/z_0] - \psi_M(z/L)\}^{-2}$ with $\kappa = 0.4$ as the von Kármán constant, z^1 is the height corresponding to U^1, and z_0 is the roughness length. For neutral conditions, with surface sensible heat flux $H_S = 0$, $\psi_M(z/L) = 0$. For the weakly convective simulations with $H_S = 10\,\mathrm{W\,m^{-2}}$, following Arya (2001) we use $\psi_M(z/L) = \ln\{[(1 + x^2)/2][(1 + x)/2]^2\} - 2\tan^{-1}(x) + \pi/2$, with $x = (1 - 15z/L)^{1/4}$. Here, $L = -u_*^3\theta_0/\kappa g H_S$ is the Obukhov length, where $\theta_0 = 300\,\mathrm{K}$, $u_* = [(\tau_{13}^s)^2 + (\tau_{23}^s)^2]^{1/4}$, and $g = 9.81\,\mathrm{m\,s^{-2}}$. Equation (4) is applied locally.

c. Model initialization and solution procedure

All simulations were initialized dry, and no cloud, radiation, or land surface models were used. The initial profile of the resolved x-velocity component was given by $u(z) = (u_*/\kappa)\ln[(z + z_0)/z_0]$, with $u_* = 0.4425\,\mathrm{m\,s^{-1}}$ and $z_0 = 0.1\,\mathrm{m}$ for $z < 500\,\mathrm{m}$, and $10\,\mathrm{m\,s^{-1}}$ above 500 m. The initial y-velocity component v was zero. Potential temperature θ was initialized to 300 K for $z < 500\,\mathrm{m}$, increasing by $4\,\mathrm{K\,km^{-1}}$ above, creating a capping inversion to prevent turbulence from reaching the model top. For the stand-alone LES, small perturbations, $\phi \in [\pm 0.5]$, obtained from a pseudorandom uniform distribution, were added to the initial values of u, v, and θ as a decreasing cubic function of height up to 500 m, to instigate turbulence.

3. Results

Results are examined after 12 h of simulated time, permitting the mesoscale inflows to the LES domains to approach equilibrium with the forcing. The coarse and fine nested LES domains were initiated at hours 8 and 10, respectively. The stand-alone LES were run for 8 h

using the LASD model, after which simulations were continued further using each of the SFS stress models.

a. Neutral flow over flat terrain

Figure 2 shows instantaneous contours of the wind speed at the beginning of hour 12, from simulations on each LES domain, from each SFS model, at approximately 97 m above the surface. While the geostrophic forcing was applied in the x direction, the orientation of the resolved structures indicates Coriolis-induced rotation near the surface.

The largest panels show the coarse LES domains (CN), which are nested within the mesoscale domain (M, not shown). The smaller panels show two different nesting strategies for the fine nested LES, the top panel showing two levels of nesting (F2N), with the fine LES nested within the coarse nested LES, and the bottom panel showing the fine LES nested directly within M (F1N). The locations of the nested LES domains are indicated by the dotted rectangles in the larger panels (also by the smaller white rectangle in Fig. 1).

The bottom panels show results from stand-alone (SA) coarse (CSA) and fine (FSA) LES, which use periodic boundary conditions directly, as described in section 2. Only results using the LASD model are shown here, for qualitative comparison. The other models' SA solutions are used in analyses described below.

Figure 2 shows that turbulence develops differently on the nested domains depending upon the SFS stress model. While each model produces turbulent flow on its corresponding CSA and FSA domains (only LASD is shown here), only the dynamic models (DRM0 and LASD) generate turbulence on any of the nested LES domains. Turbulence gradually forms on CN, before flowing into the fine LES nested within (F2N). Nesting the fine LES directly within the mesoscale domain does not yield turbulence on the fine LES domain (F1N) until a significant distance from the inflow boundaries, suggesting the utility of an intermediate coarse LES upon which turbulence can begin to form and further develop within a the finer LES. The triangular structures appearing in each nested domains are numerical artifacts of the nesting procedure that have no discernible influence once the flow becomes turbulent.

The accuracy of the turbulence appearing on the dynamic models' CN and F2N domains is evaluated using velocity spectra, resolved turbulence kinetic energy K, and resolved vertical fluxes of horizontal momentum u_*. Spectra, which show the magnitudes of various length scales within the flow, were computed for the u-velocity component, in the y direction, over grid cells $[36 \le j \le 216]$ on CN and CSA, and $[36 \le j \le 252]$ on F2N and FSA. These intervals correspond to physical distances of $L_C = 17\,820$ m and $L_F = 7128$ m on the coarse and fine LES domains, respectively, and omit bands near the y boundaries, where flow interacts with the bounding domain solution. All spectra were Hanning windowed and time averaged at 1-min increments for 2 h, yielding 120 samples.

For the nested LES domains, the y-direction spectra were computed at each x location, because of the development of turbulence with increasing distance within the nested domains. Spectra from the SA domains were likewise computed at each x location for the undulating terrain case, because of x dependence imparted by the terrain. The SA spectra from the flat terrain cases were averaged in the x direction as well because of horizontal homogeneity of the flow.

The resolved turbulence kinetic energy is defined as $K = 1/2(\overline{u'^2} + \overline{v'^2} + \overline{w'^2})$, with u', v', and w' the instantaneous deviations from mean values. Mean values were computed using all grid cells in each horizontal direction on the SA domains for the flat-terrain simulations due to the horizontal homogeneity of those flows. Mean values for the other simulations were computed in the y direction only, at each x location, using grid points $[36 \le j \le 252]$ on F2N and FSA, $[144 \le j \le 216]$ on CN, spanning 7128 m, shown by the white line in Fig. 1. The square root of the resolved covariance is given by $u_* = \sqrt{(\overline{u'w'})^2 + (\overline{v'w'})^2}$, computed analogously.

Figure 3 shows the three turbulence parameters from simulations using the two dynamic SFS stress models (LASD and DRM0), indicating the nested LES values at the x location P65, 65% of the distance between the left and right lateral boundaries of the fine LES domains (shown by the white line in Fig. 1), relative to the corresponding values from the SA domains. P65 represents a sufficient distance from the inflow boundaries for an expectation of turbulence parameters to have approached equilibrium within the nested LES domains. Data from the other SFS models are not shown since those simulations produced only trivial levels of turbulence.

Thick gray lines in Figs. 3a1,a2, and Figs. 3b1,b2 show spectra from the FSA and CSA domains, with thin black lines showing corresponding spectra from the nested LES domains, CN and F2N. Thin gray straight lines show the expected $-2/3$ slope within the inertial subrange for compensated spectra. Figures 3a3,a4, and Figs. 3b3,b4 show profiles of K and u_*, with thick gray lines showing data from the FSA domain, which is taken as the most accurate representation of the quantities. Solid and dotted black lines show the corresponding profiles at P65 from the F2N and CN domains. Profiles from CSA, which are similar to and often overlap those from FSA, and from F1N, which produced little resolved turbulence at P65, are not shown.

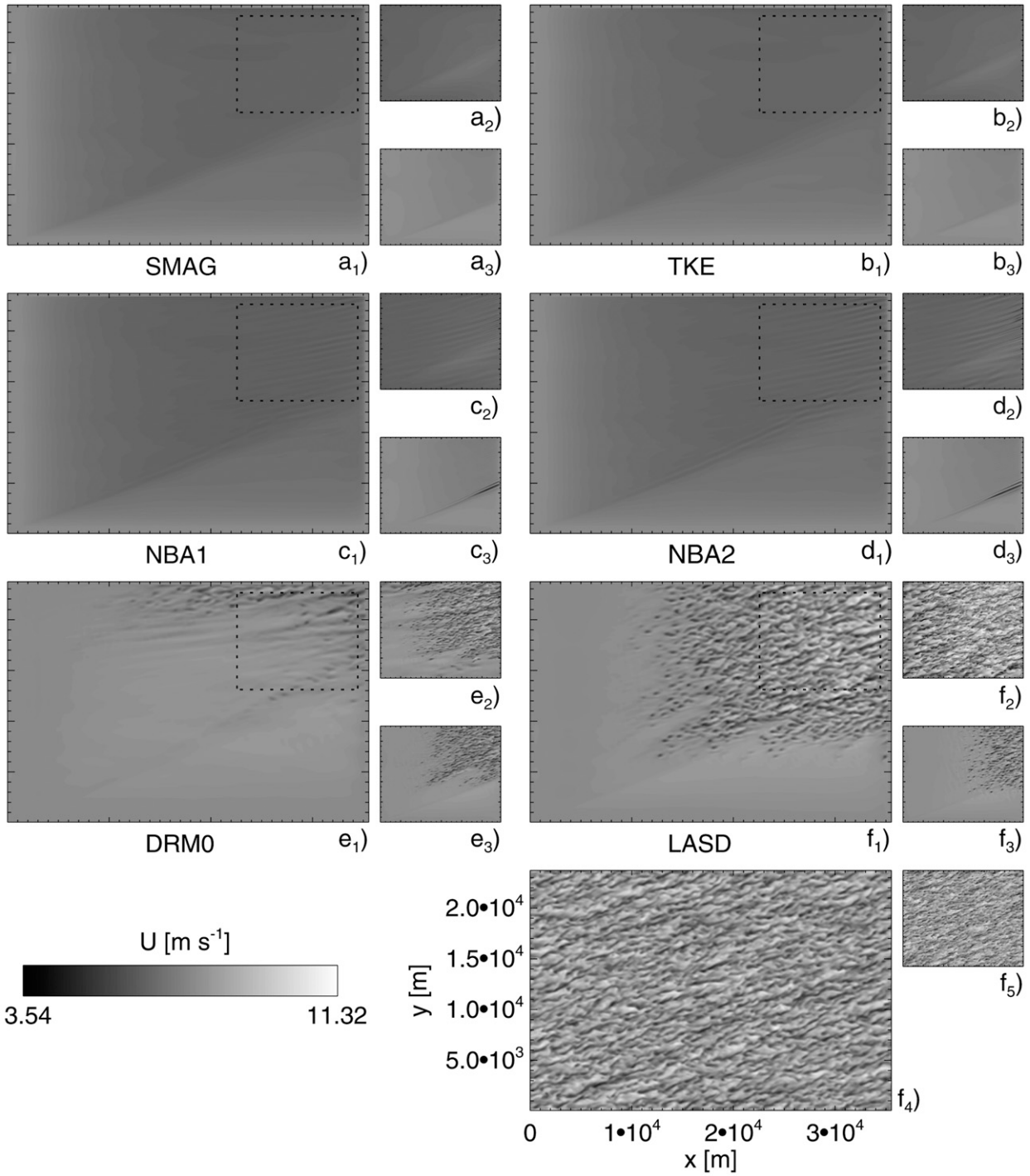

FIG. 2. Instantaneous contours of U at approximately 97 m above the surface from neutral flat terrain simulations. (top three rows) LES domains using all six SFS stress models: (large panels) the coarse nested (CN) LES domains, and (top and bottom smaller panels) fine LES domains nested within CN (F2N) and nested directly within the mesoscale domain (F1N), respectively. (bottom row) (large panel) Standalone coarse (CSA) and (small panel) fine (FSA) LES results using the LASD SFS stress model.

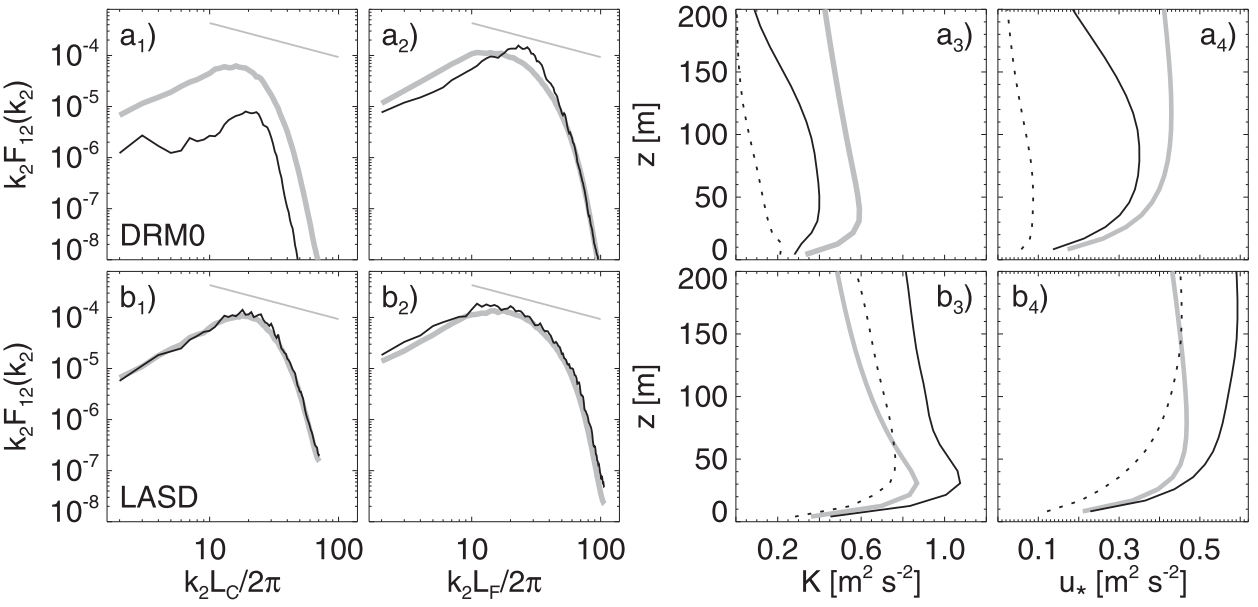

FIG. 3. Flow parameters from neutral flat terrain simulations using the DRM0 and LASD SFS stress models. (left two columns) Spectra of u taken in the y direction. Thick gray lines are from (far left) coarse stand-alone (CSA) and (middle left) fine stand-alone (FSA) LES. Black lines are from the (far left) coarse nested LES (CN) and (middle left) fine LES nested within CN (F2N). FSA and CSA spectra are averaged in time and over all x locations, those from the nested domains are time averages only, and shown at the x location P65, shown in Fig. 1. Profiles of (middle right) K and (far right) u_*. Thick gray, dotted black, and solid black lines show results from FSA, CN, and F2N, respectively. FSA profiles are time and horizontal domain averages, those from CN and F2N are averaged in time and in the y direction only, and shown at P65.

Among the two SFS models, the LASD simulation produces more rapid spectral development and better agreement between the nested and SA domains at P65. The DRM0 spectra are not well developed by the time the flow reaches P65 on CN; however, the spectra do develop fully within F2N, although power is under (over) predicted at lower (higher) frequencies. The LASD spectra show better agreement between CN and CSA than between F2N and FSA, with slightly overpredicted power on F2N.

Profiles of K and u_* show large differences between the DRM0 and LASD simulations on all domains, with differences between their SA profiles arising because of their different formulations. The agreement between the SA and nested domain solution for each model also differs, with the DRM0 nested domain solutions underpredicting K and u_*, while the LASD solution shows similar magnitudes to FSA on the CN domain, with overpredicted magnitudes on F2N. The overpredictions of turbulence parameters by the LASD solution on F2N are consistent with results from Mirocha et al. (2013), who observed similar behavior on fine LES nested with coarse LES. They hypothesized that since the smallest resolvable scales take some time to form following entry into the finer mesh, the energy producing scales are not initially connected with dissipation through a developed inertial subrange. This disconnect allows K values to increase until inertial subrange scales form, enabling the downscale energy cascade to proceed.

The disparate behaviors of the models' F2N K and u_* profiles are consistent with their spectral differences. As lower frequencies indicate larger structures, which transport momentum more efficiently, and produce greater K and u_*, the LASD F2N solution appears to support relatively more of these larger structures. The peak spectral power of the DRM0 F2N solution is associated with smaller structures, which transport momentum less effectively, generating less K.

Figure 4 shows profiles of wind speed U from each model. Thick gray, dotted, and solid black lines again show the FSA, CN, and F2N solutions, respectively. Here two additional profiles are shown. Short dashed black lines show domain-averaged profiles from M, indicating the inflow/outflow profiles for CN. Long black dashed lines show the expected logarithmic distribution (log law), computed using the surface u_* value from the corresponding FSA simulation. The M and log-law profiles agree well closer to the surface, where a logarithmic profile is expected. The departures of the FSA solutions from the log law are consistent with results from Mirocha et al. (2010) and Kirkil et al. (2012), who showed that, among the six SFS stress

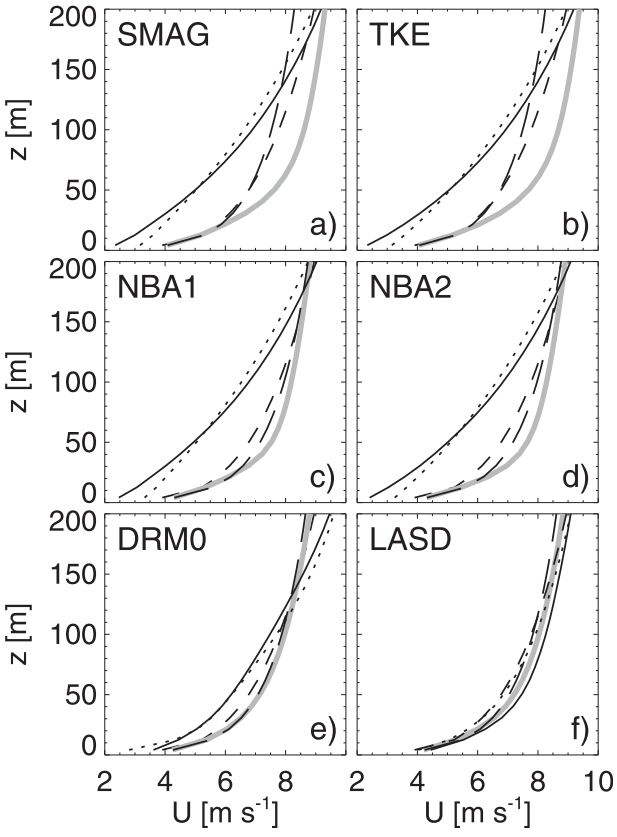

FIG. 4. (a)–(f) Profiles of U from neutral flat terrain simulations using all six SFS stress models. Thick gray, dotted black, and solid black lines show results from fine stand-alone LES (FSA), coarse nested LES (CN), and fine LES nested within CN (F2N), respectively. FSA profiles are time and horizontal domain averages, while those from CN and F2N are averaged in time and in the y direction only, and shown at the x location P65, shown in Fig. 1. Short dashed lines show the time and horizontal domain averaged mesoscale profile. Long dashed lines show the expected logarithmic profiles, computed from the time and horizontal domain averaged surface u_* value from each models' FSA domain.

models, the LASD and DRM0 models agreed most closely with the log law, followed by NBA1 and NBA2, then SMAG and TKE, for these forcing conditions. The poor agreement here between the F2N and FSA U profiles from the SMAG, TKE, and NBA models reflects the absence of resolved turbulence on F2N, conditions under which LES SFS stress models are not designed to operate.

b. Neutral flow over hilly terrain

Neutral flow over flat terrain is challenging for nested simulations as, absent instabilities or surface features to distort the flow, turbulence must form from small inhomogeneities, a slow process. We investigate the effects of undulating terrain on turbulence formation, using small sinusoidal hills and valleys, with wavelengths of 2.4 km (as shown in Fig. 1) and maximum slopes of $\pm 10°$. While steeper slopes would accelerate turbulence generation, we sought to test the models under weak terrain forcing.

Figure 5 shows contours of U, as in Fig. 2, from simulations of flow over undulating terrain. In contrast with the flat terrain case, here turbulent motions appear to form on each nested domain. Formation is most rapid for the DRM0 and LASD models. Turbulence again develops much more rapidly on F2N than on F1N, indicating the utility of a coarse LES bounding the fine LES.

Figures 6 and 7 show spectra and profiles of U, K, and u_*, as in Figs. 3 and 4. Results from all six SFS stress models are shown, as each produced some turbulence on nested domains in the presence of terrain. Spectra are computed over the same grid points in the y direction as for the flat terrain case, and profiles for all domains are averaged in the y direction over the three periods of terrain undulations shown by the white vertical line in Fig. 1. The SA spectra and profiles are not averaged in the i direction, as the terrain features impart x dependence to these parameters.

Figure 6 shows spectra and profiles at P65, which is aligned with the peaks and valleys of the undulations in the y direction (see Fig. 1). Figure 7 shows corresponding data one-quarter of a wavelength upstream, aligned with the minima of terrain undulations in the y direction. Data from the two x locations show very different distributions. The FSA, F2N, and CSA spectra at P65 generally show two distinct peaks, with the lowest-frequency peaks at $k_2 L_F/2\pi \cong 3$ on FSA and F2N, and $k_2 L_C/2\pi \cong 8$ on CN and CSA, corresponding to the number of terrain undulations captured within the different footprints over which spectra were computed on the coarse and fine LES domains. The higher-frequency peaks correspond to the largest resolved turbulence features in the flow. The spectral peaks associated with the terrain features are virtually nonexistent at the upstream location (Fig. 6) on CSA and FSA, with only vestiges appearing on F2N.

While the spectra on FSA and F2N appear similar for all simulations, larger differences are observed on CN, with only the dynamic models producing smooth distributions at higher wavenumbers on CN. The NBA models show the slowest development of turbulence spectra on CN. The NBA2 model was unstable for this case using the default value of $C_b = 0.36$. Results shown in Figs. 6 and 7 were obtained using $C_b = 0.18$, which decreased contributions from the nonlinear terms, increasing the mean dissipation rate and stabilizing the solution.

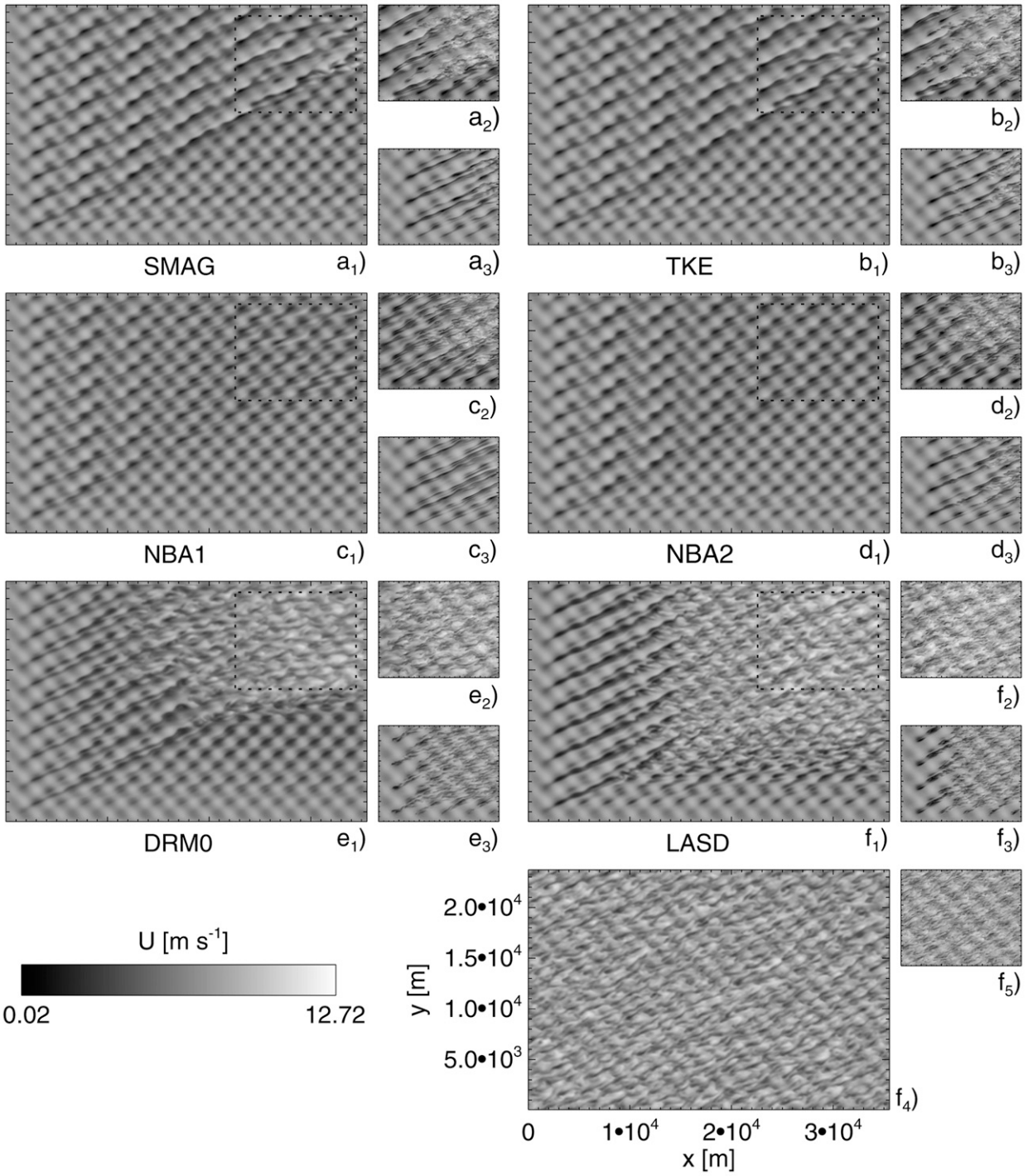

FIG. 5. Instantaneous contours of U at approximately 97 m above the surface from neutral undulating terrain simulations. (top three rows) LES domains using all six SFS stress models: (large panels) the coarse nested (CN) LES domains, and (top and bottom smaller panels) showing fine LES domains nested within CN (F2N) and nested directly within the mesoscale domain (F1N), respectively. (bottom row) (large panel) Stand-alone coarse (CSA) and (small panel) fine (FSA) LES results using the LASD SFS stress model.

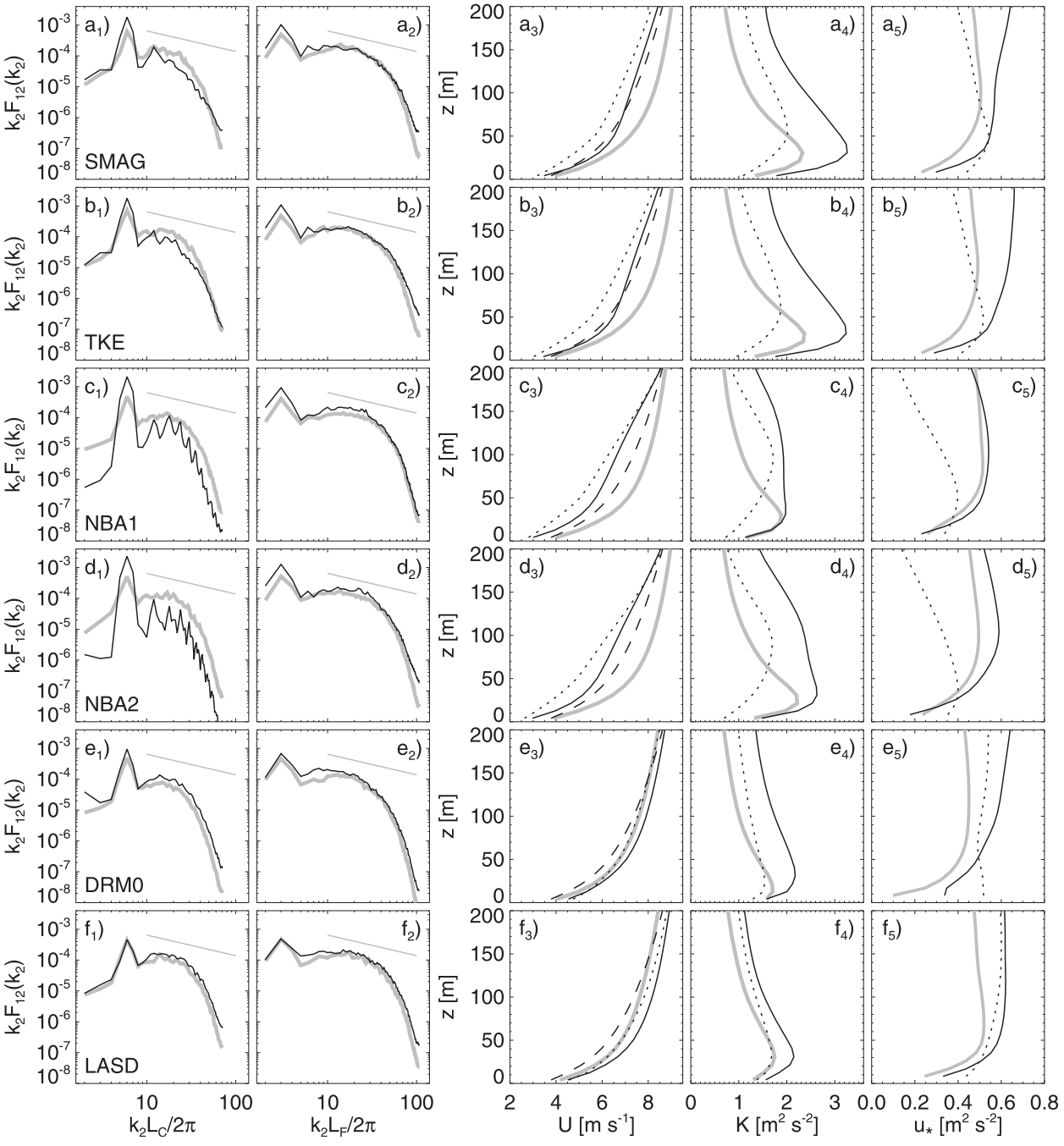

FIG. 6. Flow parameters from neutral undulating terrain simulations using all six SFS stress models. (left two columns) Spectra of u taken in the y direction. Thick gray lines are from (far left) coarse stand-alone (CSA) and (middle left) fine stand-alone (FSA) LES. Black lines are from (far left) coarse nested LES (CN) and (middle left) fine LES nested within CN (F2N). All spectra are averaged in time, and shown at the x location P65, shown in Fig. 1. (right three columns) Profiles of U, K, and u_*, respectively. Thick gray, dotted black, and solid black lines show results from FSA, CN, and F2N, respectively. Black dashed lines show U from the mesoscale domain. All profiles are averaged in time and in the y direction, and shown at P65.

The SMAG, TKE, and NBA models generally underpredict U on CN because of undeveloped turbulence, which improperly distributes momentum (see corresponding K and u_* profiles). Upon entry into F2N, turbulence develops rapidly, leading to significant increases of K and further increases of u_*. However, these increases of K and u_* only slightly increase downward momentum transport. All simulations show reduced K

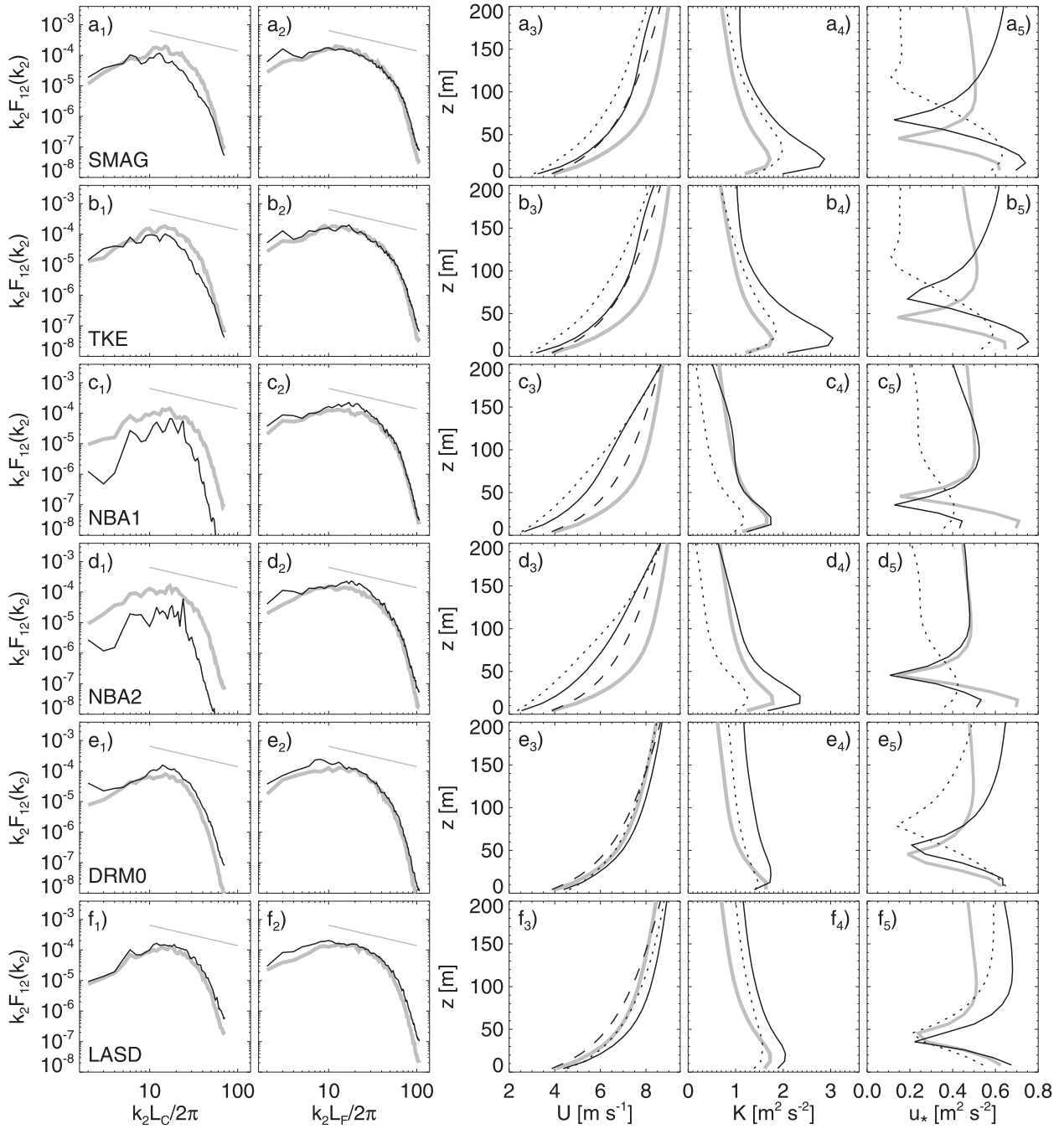

FIG. 7. Flow parameters from neutral undulating terrain simulations using all six SFS stress models. (left two columns) Spectra of u taken in the y direction. Thick gray lines are from (far left) coarse stand-alone (CSA) and (middle left) fine stand-alone (FSA) LES. Black lines are from (far left) coarse nested LES (CN) and (middle left) fine LES nested within CN (F2N). All spectra are averaged in time, and shown at the x location one-quarter of the wavelength of the undulating terrain to the left of P65, with P65 shown in Fig. 1. (right three columns) Profiles of U, K, and u_*, respectively. Thick gray, dotted black, and solid black lines show results from FSA, CN, and F2N, respectively. Black dashed lines show U from the mesoscale domain. All profiles are averaged in time and in the y direction, and shown at the same location as the spectra.

values at the upstream location relative to P65, with peaks nearer to the surface. The DRM0 K profiles peak closer to the surface than the other models. Each of the simulations capture elevated u_* minima on FSA and F2N, albeit with mismatches in magnitudes. The dynamic models capture the elevated u_* minima on CN as well.

c. Weakly convective flow over flat terrain

We investigate the influence of weak convective instability by adding a small surface heat flux of $H_S = 10\,\mathrm{W\,m^{-2}}$ to the flat terrain case. Figure 8 shows contours of wind speed, as in Figs. 2 and 5, from the convective simulations. The weak convection, coupled with the wind forcing, generates roll features on M that propagate into the nested domains. These features, while pronounced, only marginally accelerate the generation of smaller-scale turbulence on the nested LES domains. As with the other cases, the dynamic models enable the most rapid formation of turbulence on all domains. Again the coarse LES between M and F2N accelerates the development of turbulence on the fine nested LES domain relative to F1N.

Figure 9 shows spectra, U, K, and u_*, as in Figs. 3, 6, and 7, using all six SFS stress models. Here, the y-direction spectra on FSA, CSA, and M are also averaged in the x direction due to horizontal homogeneity of the flow. The CN spectra from all models show low-frequency peaks corresponding to the roll structures. F2N spectra show good agreement with FSA, with slightly enhanced power at the lowest frequencies, from the rolls. The dynamic models again achieved the best agreement overall between nested and SA solutions. While all u_* values on nested domains agree well with the FSA solution, K features large over predictions on F2N domains for all but the dynamic models. The SMAG and TKE F2N U profiles again show large departures from the log law.

4. Addition of perturbations near nest inflow planes

In the absence of strong forcing, turbulence generation from nonturbulent, mesoscale inflow is slow, requiring a large upwind fetch to generate turbulence at an area of interest (e.g., P65). Various methods to accelerate turbulence development exist; however, no consensus on the best practice has emerged. The addition of random perturbations (e.g., Keating et al. 2004) is the simplest method; however, the length scale of turbulence generation is typically large. Perturbation recycling and rescaling methods (e.g., Lund et al. 1998) are more efficient; however, those methods are based upon equilibrium assumptions, and require information from within the LES domain, hence, they are of limited applicability to real nested LES setups. Precursor simulations (e.g., Thomas and Williams 1999), which use a separate LES to develop turbulence, can provide more accurate turbulent inflow; however, significant additional computation is required, and the precursor domain may not reflect the upwind fetch in a real nested LES setup.

Given the absence of a consensus on the best approach and the unique requirements of using realistic mesoscale inflow to drive LES nested within, we investigate an approach that is general and simple to implement. Tendencies are added to WRF's θ, u, and v equations within the nested domains near the inflow boundaries. The tendencies are chosen with the goal of providing the minimal disturbance to the flow field upon which turbulence can develop naturally based on the forcing as it proceeds downstream.

Figure 10 shows the spatial pattern of the perturbation tendencies, with light and dark indicating positive and negative values. The top and bottom panels show x–y and x–z planes, respectively. The perturbations begin 12 grid points inside the inflow planes, to maintain some distance from the relaxation zones. The perturbations are sinusoidal in each direction, with periods of 24 grid points in the horizontal (period 24) and approximately 320 m in the vertical (vertical grid spacing is nonuniform) directions. The amplitudes of the tendencies decrease as the cosine of height up to approximately 640 m (32 grid points above the surface), the approximate boundary layer height from stand-alone LES of the neutral, flat terrain ABL.

a. Neutral flow over flat terrain

The search for optimal perturbations was limited, the goal being examination of the viability of the basic approach. Amplitudes of $\pm 1000\,\mathrm{kg\,s^{-4}}$ for each tendency[1] were found to work well, yielding perturbations of $(\Delta u, \Delta v; \Delta\theta) \cong \pm 2 - 3$ ($\mathrm{m\,s^{-1}}$, K). Smaller amplitudes failed to generate robust turbulence structures, while larger amplitudes produced very large structures that spawned little smaller-scale turbulence (not shown). Perturbations much smaller than 24 grid points failed to produce robust turbulence within CN, while those much larger spawned smaller scales slowly (not shown). The sign of each tendency was reversed every 1200 s on CN to limit the extents of correlated perturbations. While a distribution of perturbation sizes and amplitudes would likely further accelerate turbulence generation, this simple method produced encouraging results.

1) PERTURBATIONS USING THE LASD MODEL

As the LASD model provided the best overall performance on nested domains, we use it to examine four

[1] The tendencies for WRF's prognostic variables are multiplied by column mass (in units of Pa).

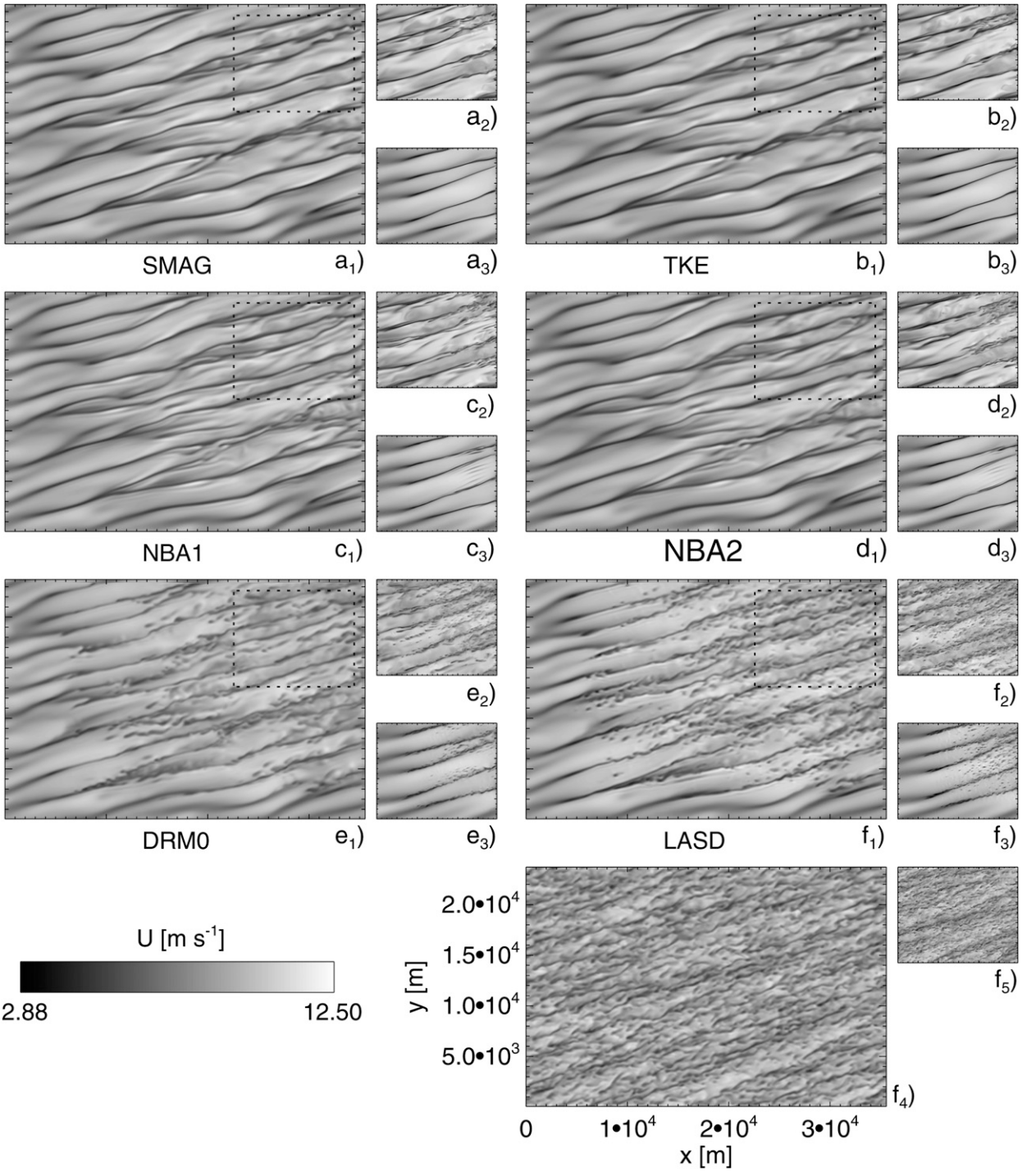

FIG. 8. Instantaneous contours of U at approximately 97 m above the surface from weakly convective flat terrain simulations. (top three rows) LES domains using all six SFS stress models: (large panels) the coarse nested (CN) LES domains, and (top and bottom smaller panels) fine LES domains nested within CN (F2N) and nested directly within the mesoscale domain (F1N), respectively. (bottom row) (large panel) Stand-alone coarse (CSA) and (small panel) fine (FSA) LES results using the LASD SFS stress model.

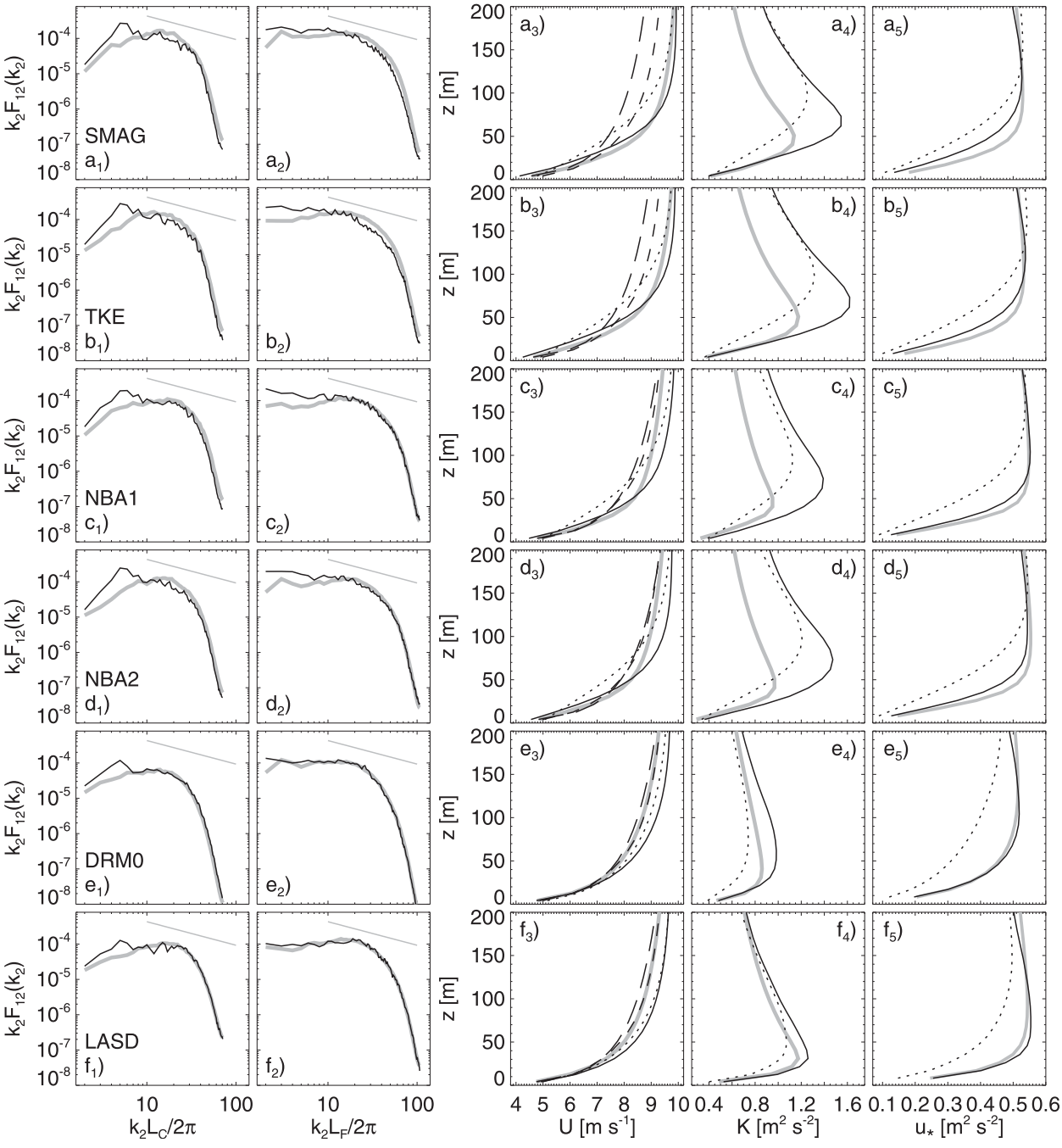

FIG. 9. Flow parameters from weakly convective flat terrain simulations using all six SFS stress models. (left two columns) Spectra of u taken in the y direction. Thick gray lines are from (far left) coarse stand-alone (CSA) and (middle left) fine stand-alone (FSA) LES. Black lines are from (far left) coarse nested LES (CN) and (middle left) fine LES nested within CN (F2N). FSA and CSA spectra are averaged in time and over all x locations, those from the nested domains are time averages only, and shown at the x location P65, shown in Fig. 1. (right three columns) Profiles of U, K, and u_*, respectively. Thick gray, dotted black, and solid black lines show results from FSA, CN, and F2N, respectively. Short dashed lines show the mesoscale (M) U profile. Long dashed lines show the expected logarithmic U profiles, computed from the surface u_* values from each models' FSA domain. The M and FSA profiles are time and horizontal domain averages while those from CN and F2N are averaged in time and in the y direction only, and shown at P65.

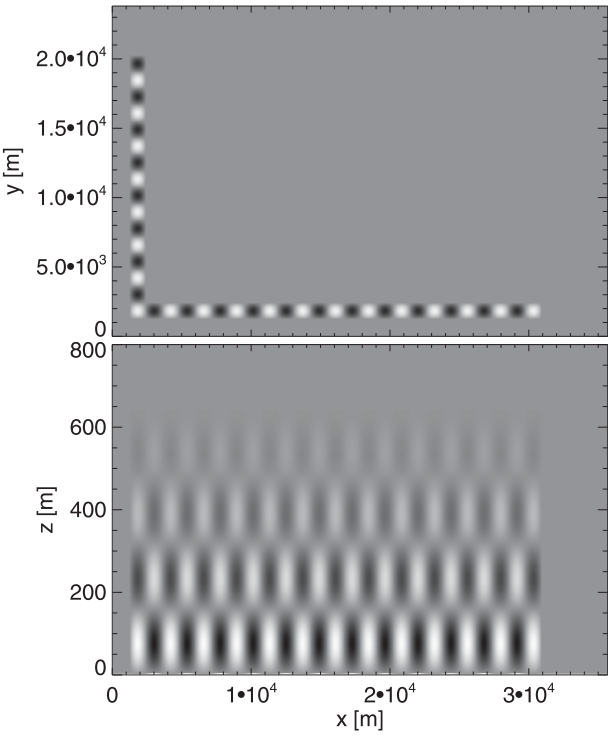

FIG. 10. Spatial pattern of perturbation tendencies added to θ, u, and v. Periods of oscillations shown here span 24 grid points in each horizontal direction (where grid spacing is uniform), with two periods used between the surface and approximately 640 m in the vertical direction (which uses a stretched grid), with magnitudes attenuating with height. Light and dark shades indicate positive and negative perturbations (although the tendencies alternate in sign during simulations).

perturbation strategies. We begin with neutral flow over flat terrain. Figure 11 shows spectra and U, u_*, and K profiles, as in Figs. 6–8, with the top panels showing the nonperturbed simulation (NO P) for comparison. Each subsequent row of panels in Fig. 11 show the impacts of adding perturbations, as described in the left column. Applying perturbations to CN creates subtle changes to the CN spectra, slightly reducing agreement with those from CSA. However, the spectra on F2N show improved agreement with those from FSA, with slightly lower energies at low frequencies. Perturbations on CN have much more profound effects on K and u_* on F2N, showing substantial improvements at P65. The additions of perturbations on F2N as well as CN (P24 CN, P24 F2N and P24 CN, P8 F2N) result in comparatively small changes at P65 relative to perturbations on CN only (P24 CN). For the smaller perturbations on F2N (P24 CN, P8 F2N), the time period of the sign reversal of the perturbation tendencies was reduced to 200 s on F2N, consistent with the reduction in spatial scale. Adding small perturbations to only F2N only (P8 F2N) yields only small improvements at P65 compared with the no perturbation (NO P) case.

While Fig. 11 shows profiles at one location within F2N, these quantities change as the flow traverses the extent of the F2N domain. Figure 12 shows values of K (top), u_* (middle), and U (bottom) at 97 m above the surface, as a function of distance in the x direction (i index), for each simulation shown in Fig. 11. Thick gray lines show the FSA solution. Thin vertical gray lines show P65. Values from the last eight grid points within F2N are omitted because of nonphysical variability induced by the relaxation procedure.

Consistent with the profiles at P65 shown in Fig. 11, the simulations not using perturbations on CN most strongly overpredict K and u_* throughout all of F2N. Adding period 24 perturbations to CN significantly reduces these overpredictions. The effects of also adding perturbations to F2N depend upon their sizes. While Fig. 11 suggested little difference between adding period 24 versus period 8 perturbations on F2N, Fig. 12 shows that the close agreement of the two solutions at P65 is not uniform across F2N. The larger perturbations create overpredictions of K that attenuate gradually, while smaller perturbations produce lower, steadier values more quickly. Adding perturbations of period 8 to only F2N had little effect on the solution.

We hypothesize that the disparate effects of perturbations of different sizes on F2N are related to their impacts on the cascade process. Assuming an effective mesh resolution of $\approx 6 - 7\Delta x$ [due to attenuation of the smallest resolvable scales by the discrete numerical solution procedure, see e.g., Skamarock (2004)], flow entering F2N contains resolved scales of similar sizes to the period 24 perturbations imposed within F2N. In contrast, period 8 perturbations on F2N trigger smaller-scale motions not resolved within the inflow. These smaller scales fall within the inertial subrange of the resolved turbulence advecting into F2N, and, via interactions with the resolved turbulence, accelerate formation of the downscale energy cascade.

The overpredictions of u_* and K on F2N in the nonperturbed simulations are reduced when perturbations are added to CN. Adding perturbations to CN reduces K values at the point where flow enters F2N, after which K increases within F2N via the mechanism described in section 3. Upon reaching P65, agreement between F2N and FSA is quite good. Adding small perturbations also within F2N reduces K values slightly via faster development of the downscale cascade.

The perturbations influence U differently than K and u_*. In the absence of perturbations on CN, U increases rapidly upon entry into F2N. This, we hypothesize, results from the turbulence on CN still developing,

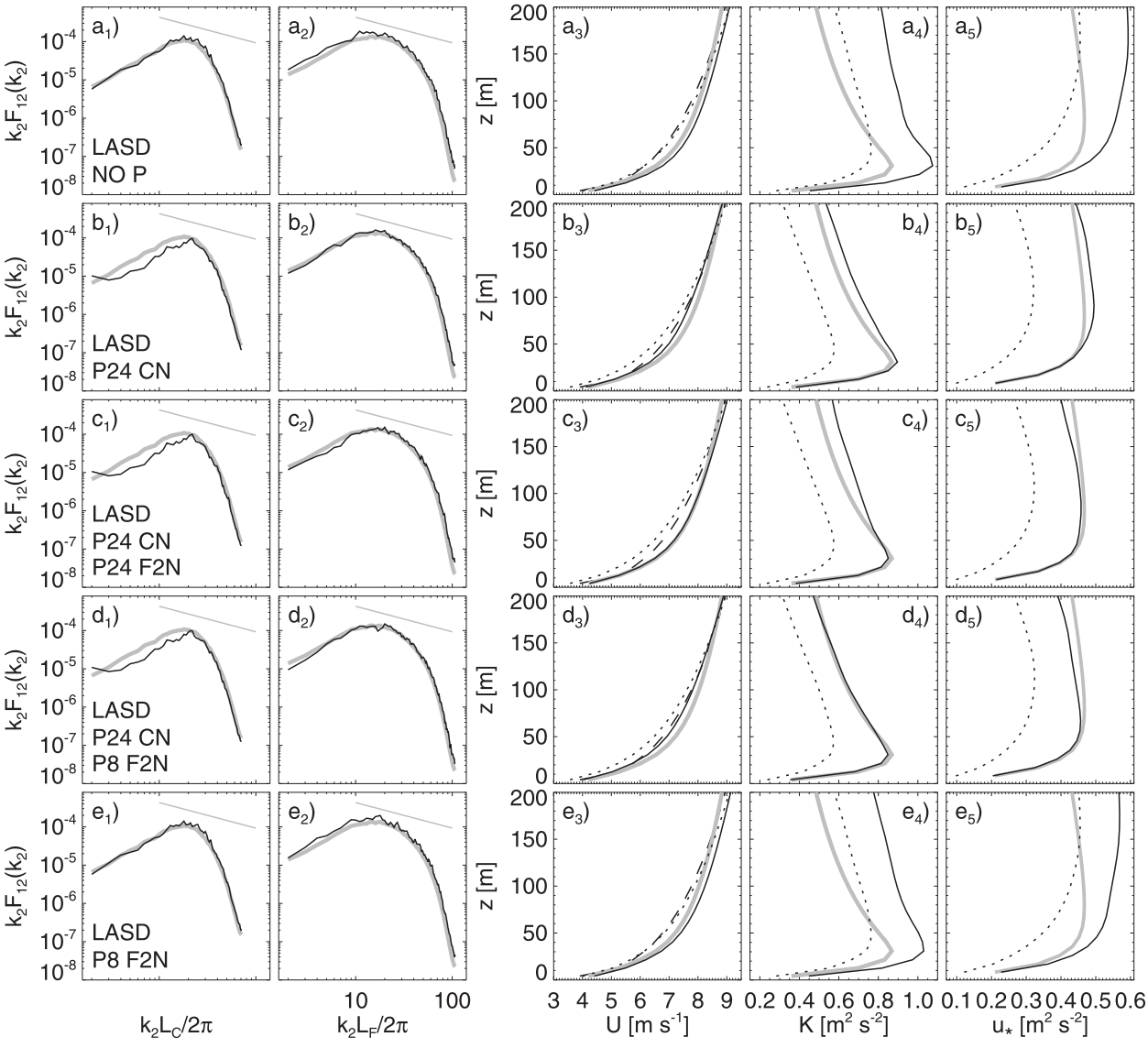

FIG. 11. Flow parameters from neutral flat terrain simulations using the LASD SFS stress model, showing the impact of adding perturbations with spatial extents of 24 (P24) and 8 (P8) grid points in each horizontal direction, as shown in Fig. 10, (far left panels) to the coarse nested LES (CN) and fine LES nested within CN (F2N), respectively. (left two columns) Spectra of u taken in the y direction. Thick gray lines are from (far left) coarse stand-alone (CSA) and (middle left) fine stand-alone (FSA) LES. Black lines are from (far left) coarse nested LES (CN) and (middle left) fine LES nested within CN (F2N). FSA and CSA spectra are averaged in time and over all x locations, those from the nested domains are time averages only, and shown at the x location P65, shown in Fig. 1. (right three columns) Profiles of U, K, and u_*, respectively. Thick gray, dotted black, and solid black lines show results from FSA, CN, and F2N, respectively. Black dashed lines show U from the mesoscale domain. The M and FSA profiles are time and horizontal domain averages, while those from CN and F2N are averaged in time and in the y direction only, and shown at P65.

therefore, not yet possessing correlations that properly transport momentum. However, as turbulence continues to develop on F2N, those correlations strengthen rapidly in the absence of smaller scales that have not yet formed, and are required for the energy cascade to proceed. The results are overprediction of both K and u_*, consistent with rapid downward transport of momentum, and overpredictions of U in the lower ABL.

Of the simulations using perturbations on CN, those that also use the large perturbations on F2N (P24 CN, P24 F2N) create the largest overpredictions of U. The first local U maximum nearest to the left inflow plane likely reflects entrainment of higher-momentum air from aloft resulting from the large perturbations. The second, broader U maximum likely reflects those perturbations leading to excessive K and u_* and increased

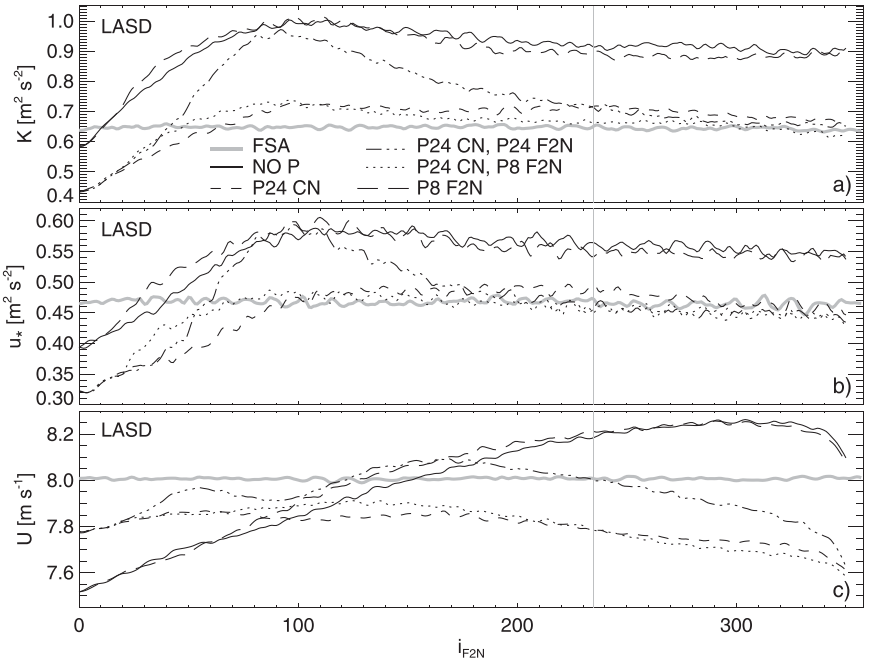

FIG. 12. (a) K, (b) u_*, and (c) U values at 97 m above the surface as functions of distance in the x direction (i grid point) within fine LES nested within coarse nested LES (F2N), from the five simulations shown in Fig. 11. Thick gray lines show the time and horizontal domain averaged fine stand-alone LES (FSA) solution. Other lines show time and y-direction averages from F2N. Solid black lines show results using no perturbations. Other black lines show results of adding perturbations with spatial extents of 24 (P24) and 8 (P8) grid points in each horizontal direction (as shown in Fig. 10) to the coarse nested LES (CN) and F2N, as specified in the legend in the top panel. The thin vertical line shows the x location P65, as in Fig. 1.

downward momentum transport. However, the large perturbations on F2N also accelerate formation of inertial subrange scales, which dissipate K and decrease downward momentum transport relative to the NO P and P24 CN cases.

Adding smaller period 8 perturbations on F2N (P24 CN, P8 F2N) has a muted effect compared to the P24 CN case, slightly accelerating the rate of increase of K and u_*, but curtailing the overpredictions slightly as well. Comparison with the P24 CN, P24 F2N case suggests that the smaller period 8 perturbation results trigger scales of motion mainly in the inertial subrange.

2) PERTURBATIONS USING ALL SIX SFS STRESS MODELS

As perturbations of period 24 on CN and 8 on F2N produced among the best overall results using the LASD model, these perturbations were applied using all six SFS stress models. Figure 13 shows instantaneous U contours from neutral flow over flat terrain, as in Fig. 2, with the bottom panels again showing (nonperturbed) LASD solutions from CSA and FSA. The SFS stress model strongly influences how the perturbations evolve on CN. The SMAG, TKE, and NBA models produce elongated streaks throughout CN, while the dynamic models more rapidly produce smaller structures. The top smaller panels (top three rows) show the F2N solutions with no perturbations on F2N, while the bottom smaller panels include period 8 perturbations on F2N in addition to the perturbations on CN. Each F2N solution produces smaller-scale turbulence, with the dynamic models the most rapid. The addition of small perturbations on F2N slightly accelerates development of smaller scales.

Figure 14 shows the results of perturbations on spectra and U, K, and u_* profiles using all six SFS stress models. Here, while only the LASD solution shows a developed spectrum on CN, all F2N spectra show a developed spectrum, with all but the LASD showing peaks of various sizes associated with the perturbation period.

While the LASD model shows good agreement between the F2N and FSA profiles at P65, other models show larger discrepancies. Period 24 perturbations were applied to only the CN domains using the other models (not shown); however, results were worse overall than when perturbations were used on both domains, except

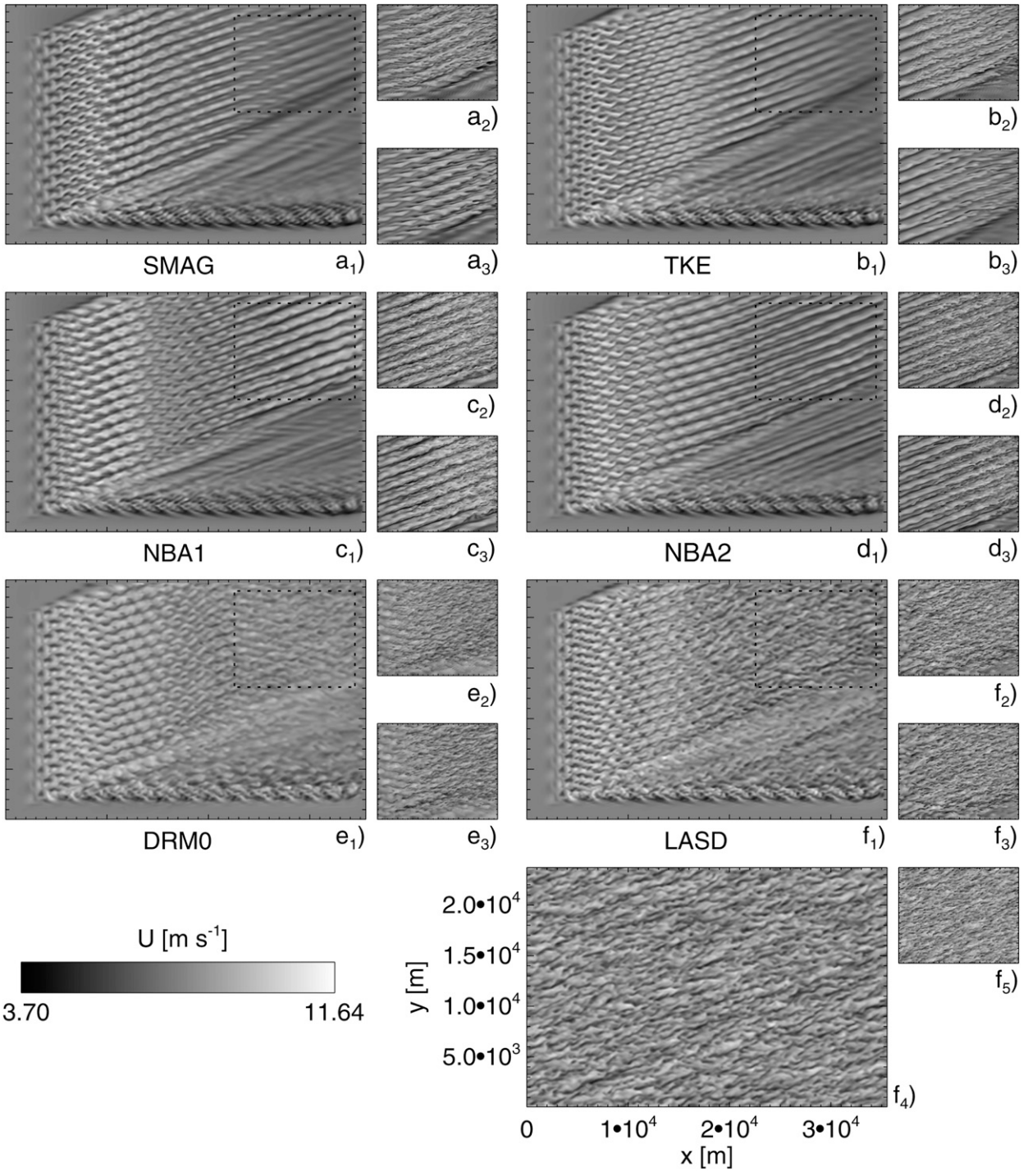

FIG. 13. Instantaneous contours of U at approximately 97 m above the surface from neutral flat terrain simulations with perturbations. (top three rows) LES domains using all six SFS stress models: (large panels) showing the coarse nested (CN) LES domains. Perturbations with spatial extents of 24 grid points in each horizontal direction, as shown in Fig. 10, were applied on CN. (smaller panels) Fine LES domains nested within CN (F2N). (small top-right panels) Used additional perturbations with spatial extents of 8 grid points in each horizontal direction on F2N, while (small bottom-right panels) show the F2N solution with no additional perturbations beyond those applied on CN. (bottom row) (large panel) CSA and (small panel) FSA solutions.

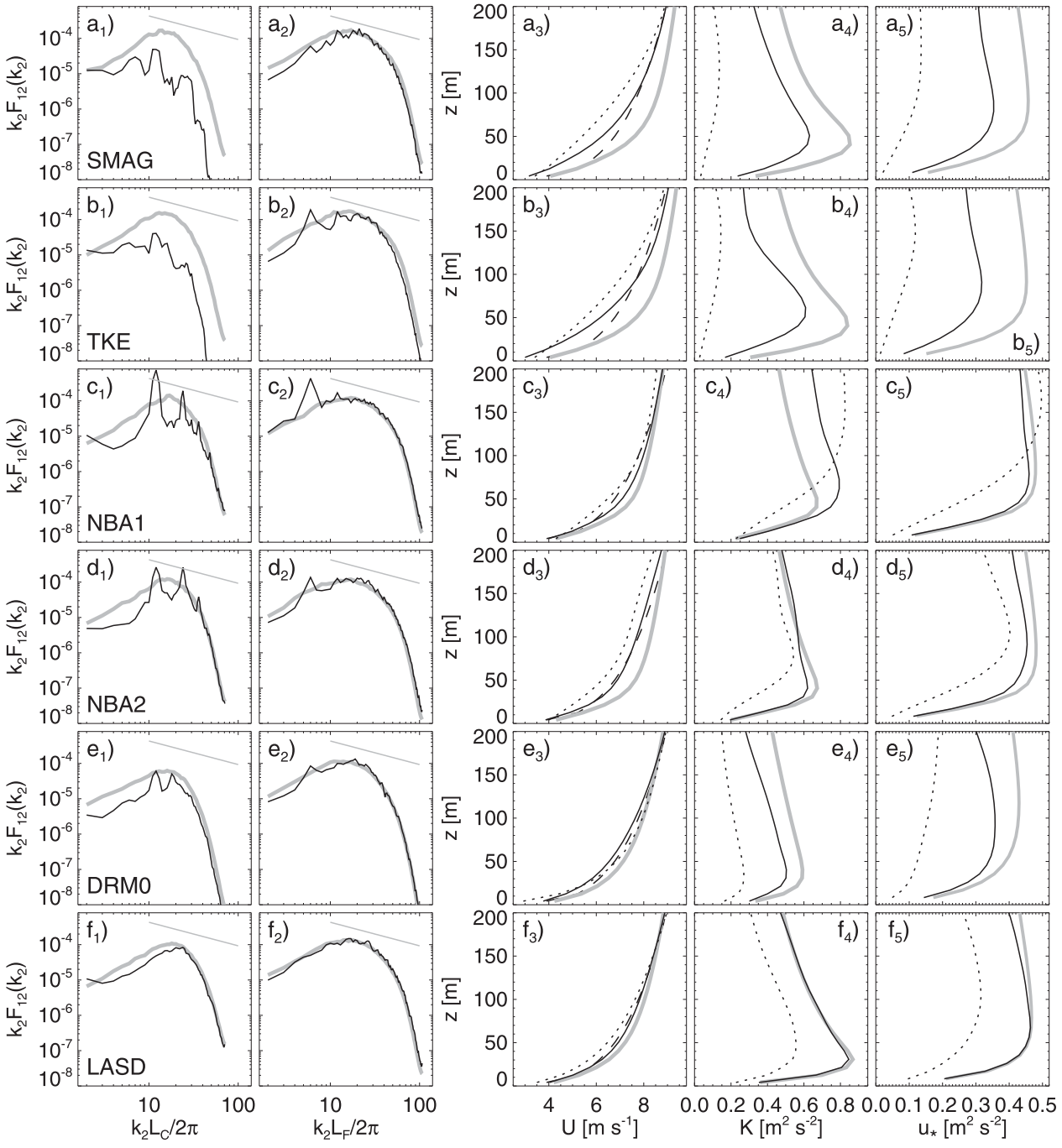

FIG. 14. Flow parameters from neutral flat terrain simulations using all six SFS stress models, using perturbations with spatial extents of 24 grid points in each horizontal direction on the coarse nested LES (CN), and 8 grid points on fine LES nested within CN (F2N), respectively. (left two columns) Spectra of u taken in the y direction. Thick gray lines are from (far left) coarse stand-alone (CSA) and (middle left) fine stand-alone (FSA) LES. Black lines are from the (far left) coarse nested LES (CN) and (middle left) fine LES nested within CN (F2N). FSA and CSA spectra are averaged in time and over all x locations, those from the nested domains are time averages only, and shown at the x location P65, shown in Fig. 1. (right three columns) Profiles of U, K, and u_*, respectively. Thick gray, dotted black, and solid black lines show results from FSA, CN, and F2N, respectively. Black dashed lines show U from the mesoscale domain. The M and FSA profiles are time and horizontal domain averages while those from CN and F2N are averaged in time and in the y direction only, and shown at P65.

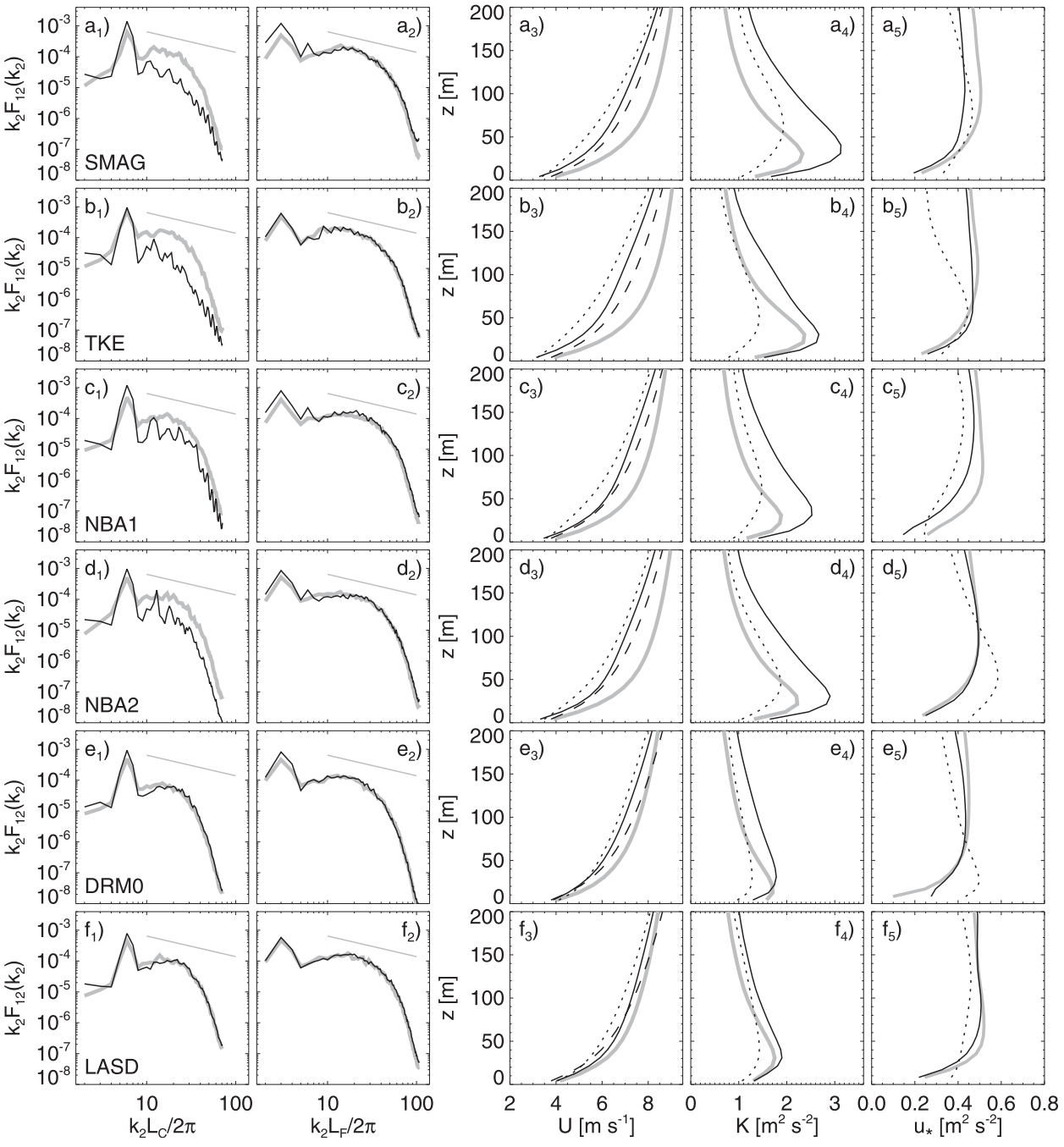

FIG. 15. Flow parameters from neutral undulating terrain simulations using all six SFS stress models, using perturbations with spatial extents of 24 grid points in each horizontal direction on the coarse nested LES (CN), and 8 grid points on fine LES nested within CN (F2N), respectively. (left two columns) Spectra of u taken in the y direction. Thick gray lines are from (far left) coarse stand-alone (CSA) and (middle left) fine stand-alone (FSA) LES. Black lines are from (far left) coarse nested LES (CN) and (middle left) fine LES nested within CN (F2N). All spectra are averaged in time, and shown at the x location P65, shown in Fig. 1. (right three columns) Profiles of U, K, and u_*, respectively. Thick gray, dotted black, and solid black lines show results from FSA, CN, and F2N, respectively. Black dashed lines show U from the mesoscale domain. All profiles are averaged in time and in the y direction, and shown at P65.

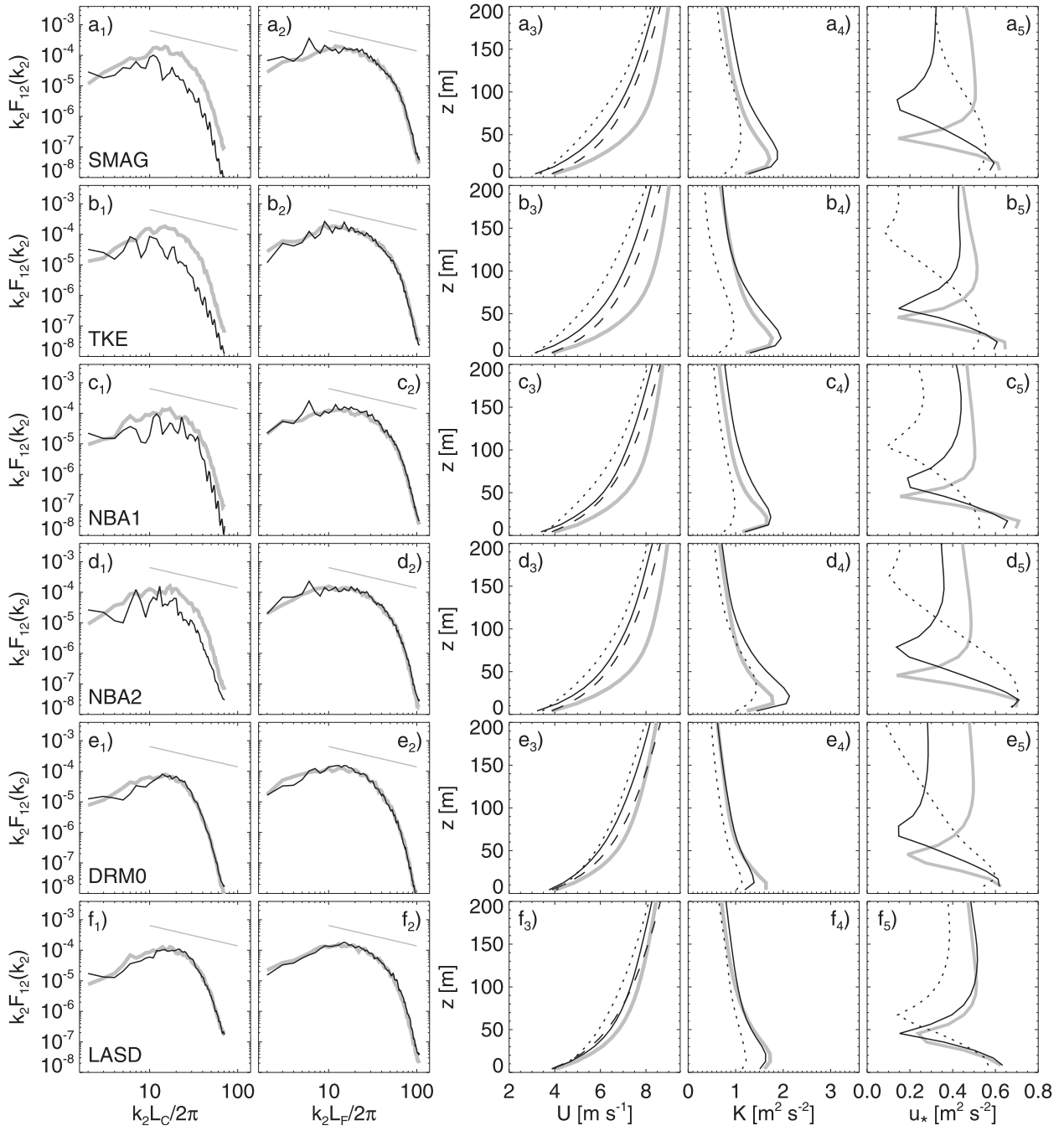

FIG. 16. Flow parameters from neutral flow over undulating terrain simulations using all six SFS stress models, using perturbations with spatial extents of 24 grid points in each horizontal direction on the coarse nested LES (CN), and 8 grid points on fine LES nested within CN (F2N), respectively. (left two columns) Spectra of u taken in the y direction. Thick gray lines are from (far left) coarse stand-alone (CSA) and (middle left) fine stand-alone (FSA) LES. Black lines are from (far left) coarse nested LES (CN) and (middle left) fine LES nested within CN (F2N). All spectra are averaged in time, and shown at the x location one-quarter of the wavelength of the undulating terrain to the left of P65, with P65 shown in Fig. 1. (right three columns) Profiles of U, K, and u_*, respectively. Thick gray, dotted black, and solid black lines show results from FSA, CN, and F2N, respectively. Black dashed lines show U from the mesoscale domain. All profiles are averaged in time and in the y direction, and shown at the same location as the spectra.

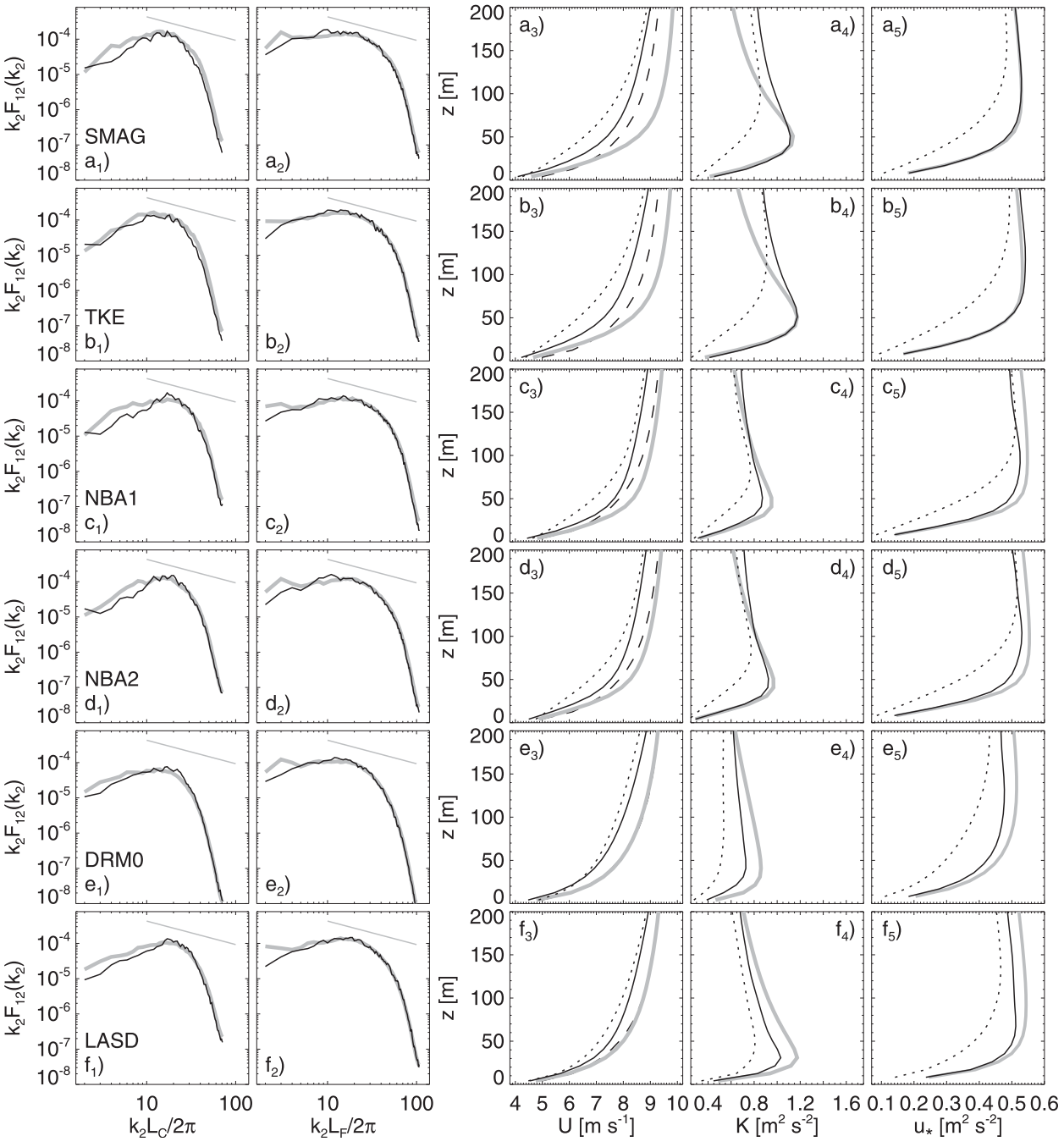

FIG. 17. Flow parameters from weakly convective flat terrain simulations using all six SFS stress models, using perturbations with spatial extents of 24 grid points in each horizontal direction on the coarse nested LES (CN), and 8 grid points on fine LES nested within CN (F2N), respectively. (left two columns) Spectra of u taken in the y direction. Thick gray lines are from (far left) coarse stand-alone (CSA) and (middle left) fine stand-alone (FSA) LES. Black lines are from (far left) coarse nested LES (CN) and (middle left) fine LES nested within CN (F2N). FSA and CSA spectra are averaged in time and over all x locations, those from the nested domains are time averages only, and shown at the x location P65, shown in Fig. 1. (right three columns) Profiles of U, K, and u_*, respectively. Thick gray, dotted black, and solid black lines show results from FSA, CN, and F2N, respectively. Black dashed lines show U from the mesoscale domain. The M and FSA profiles are time and horizontal domain averages while those from CN and F2N are averaged in time and in the y direction only, and shown at P65.

for DRM0, which performed slightly better. Adding period 8 perturbations to F2N greatly reduces the overpredictions of K from the SMAG, TKE, and NBA models relative to perturbations on CN only, by providing scales of motions near the inertial subrange, accelerating the downscale energy cascade. Small perturbations on F2N have lesser effects when using the dynamic models, which develop smaller scales quite readily on their own.

b. *Neutral flow over hilly terrain*

Figures 15 and 16 show the results of adding perturbations of period 24 on CN and period 8 on F2N to the hilly terrain simulations. Comparison with the nonperturbed simulations (Figs. 6 and 7) shows generally improved agreement between the F2N and FSA spectra and profiles, even as the spectra on CN develop more slowly.

c. *Weakly convective flow over flat terrain*

Figure 17 shows results from the weakly convective simulations using perturbations of period 24 on CN and period 8 on F2N. Comparison with the nonperturbed simulation (Fig. 9) shows either improvement or degradation, depending upon the model. While the SMAG, TKE, and NBA simulations show improved K and u_* values on F2N, those of U are worse. The dynamic models' U, K, and u_* values on F2N are all degraded slightly when perturbations are added. Weak convection enables the dynamic models to spontaneously generate well-developed turbulence. The addition of the perturbations investigated herein to either or both domains (not shown) interferes with the naturally developing turbulence, degrading the results.

5. Summary and conclusions

Under the relatively weak forcing conditions examined herein, nesting from a mesoscale simulation down to LES using WRF's extant nesting strategy did not reliably produce turbulence fields that resembled those from stand-alone LES using periodic lateral boundary conditions. For neutral flow over flat terrain, while all six SFS stress models produced realistic turbulence on stand-alone (periodic) domains, only the two dynamic models (LASD and DRM0) produced turbulence on nested LES domains. Adding small terrain features (wavelengths of 2.4 km and maximum slopes of 10°) accelerated turbulence formation, resulting in some turbulence on nested LES domains using all six models. However, the u-velocity spectra, wind speed, and resolved components of the turbulence kinetic energy and friction velocity were not well predicted on the nested LES. Adding a small surface heat flux ($10\,\mathrm{W\,m^{-2}}$) to the flat terrain simulations further accelerated turbulence production on nested domains. While the dynamic models provided good performance under weakly convective conditions, the other models continued to produce considerable errors in some or all of the examined flow parameters.

The dynamic models, by locally reducing dissipation rates, allowed turbulence to develop most rapidly, producing superior performance on nested domains. Other models contain parameters that could potentially be modified to accelerate turbulence formation.

Adding small thermal and velocity perturbations near the inflow boundaries of nested LES domains accelerated turbulence formation and improved nested LES results, except for the dynamic models under weakly convective condition, which produced good results without perturbations. For the coarse LES nested within the mesoscale simulations, perturbations with periods of 24 grid cells produced the best results among those investigated. For fine LES nested within coarse LES, smaller perturbations (periods of 8 grid cells) were superior, by seeding scales near the inertial subrange of the larger eddies advecting in from the bounding domain, accelerating the downscale energy cascade.

Nesting a fine LES domain within a coarser surrounding LES, upon which turbulence can begin to develop, was found superior to nesting it directly within the mesoscale simulation, irrespective of perturbation approaches applied.

Considerable differences were observed in the effects of perturbations on the various SFS stress models. Each model likely possesses a unique optimal perturbation approach. The effects of perturbations vary with stability, affording generally greater benefits during neutral than convective conditions. Real atmospheric flows are seldom neutral; however, they are often weakly stable and still turbulent, a context for which perturbations would be expected to have similar results to the neutral cases examined herein. While our initial results are encouraging, further exploration of these issues is needed to establish a robust framework for downscaling mesoscale flows to LES under variable forcing conditions using WRF.

Acknowledgments. We thank Tina Chow and Elie Bou-Zeid for many helpful discussions. This work was performed under the auspices of the U.S. Department of Energy by Lawrence Livermore National Laboratory under Contract DE-AC52-07NA27344, and was supported by both the Laboratory Directed Research and

Development program, and the U.S. DOE Office of Energy Efficiency and Renewable Energy.

APPENDIX

Details of SFS Stress Model Formulations

a. Constant-coefficient Smagorinsky model (SMAG)

The SMAG model (Smagorinsky 1963; Lilly 1967) is given by

$$\tau_{ij} = -2K_M \tilde{S}_{ij}, \tag{A1}$$

where, in WRF,

$$K_M = (C_S l)^2 \max(0, |\tilde{S}_{ij}| - P_r^{-1} N^2) \tag{A2}$$

is the eddy viscosity coefficient for momentum, $C_S = 0.18$ is a constant, $l = (\Delta x \Delta y \Delta z)^{1/3}$ is a length scale (isotropic), $\tilde{S}_{ij} = 1/2[(\partial \tilde{u}_i/\partial x_j) + (\partial \tilde{u}_j/\partial x_i)]$ is the resolved strain-rate tensor, N^2 is the Brunt–Väisälä frequency, and $P_r^{-1} = 3$ is the inverse of the turbulent Prandtl number. Tildes denote the low-pass filtered, or resolved component of the flow.

Scalar fluxes are given by

$$S_j = -2K_q \frac{\partial \tilde{q}}{\partial x_j}, \tag{A3}$$

where K_q is the eddy viscosity coefficient for scalar q, given by $K_q = P_r^{-1} K_M$.

b. 1.5-order TKE model (TKE)

The 1.5-order TKE model (e.g., Deardorff 1972) uses

$$K_M = C_K l \sqrt{e} \tag{A4}$$

in place of Eq. (A1). Here, $C_K = 0.1$ is a constant, and e is the SFS TKE, for which a separate equation is solved. The (isotropic) length scale is obtained from

$$l = \min[(\Delta x \Delta y \Delta z)^{1/3}, 0.76 e^{1/2} N^{-1}].$$

Scalar fluxes are obtained from Eq. (A3), with $P_r^{-1} = 3$ for the horizontal and $P_r^{-1} = 1 + 2l/\Delta z$ for the vertical values of K_H, respectively. See Skamarock et al. (2008) for further details regarding the SMAG and TKE models.

c. Lagrangian-averaged scale dependent model (LASD)

The LASD model (Bou-Zeid et al. 2005, 2008) is based upon Eqs. (A1) and (A2), with C_S replaced by a spatially and temporally varying value. The LASD model uses two spatial filters to compute two values of C_S, corresponding to two resolved scales of motion. Power-law dependence is used to extrapolate the C_S value used in Eq. (A2).

The LASD model is stabilized via Lagrangian averaging, using weighted time histories for averaged quantities along fluid path lines.

Scalar fluxes for the LASD model are computed from Eq. (A3).

d. Nonlinear backscatter and anisotropy models (NBA1 and NBA2)

The NBA models (Kosović, 1997) are based upon a nonlinear constitutive relation that includes second-order tensor products. The NBA1 model is given by

$$\begin{aligned} M_{ij} = -(C_S l)^2 \Bigg\{ & 2(2\tilde{S}_{mn}\tilde{S}_{mn})^{1/2}\tilde{S}_{ij} \\ & + C_1 \left(\tilde{S}_{ik}\tilde{S}_{kj} - \frac{1}{3}\tilde{S}_{mn}\tilde{S}_{mn}\delta_{ij} \right) \\ & + C_2(\tilde{S}_{ik}\tilde{R}_{kj} - \tilde{R}_{ik}\tilde{S}_{kj}) \Bigg\}. \end{aligned} \tag{A5}$$

The NBA2 model, which incorporates SFS TKE, is given by

$$\begin{aligned} M_{ij} = -C_e l \Bigg\{ & 2(e)^{1/2}\tilde{S}_{ij} + \left(\frac{27}{8\pi}\right)^{1/3} \\ & \times C_s^{2/3} l \left[C_1 \left(\tilde{S}_{ik}\tilde{S}_{kj} - \frac{1}{3}\tilde{S}_{mn}\tilde{S}_{mn}\delta_{ij} \right) \right. \\ & \left. + C_2(\tilde{S}_{ik}\tilde{R}_{kj} - \tilde{R}_{ik}\tilde{S}_{kj}) \right] \Bigg\}. \end{aligned} \tag{A6}$$

Here, $\tilde{R}_{ij} = 1/2[(\partial \tilde{u}_i/\partial x_j) - (\partial \tilde{u}_j/\partial x_i)]$ is the resolved rotation-rate tensor, $C_S = [8(1 + C_b)/27\pi^2]^{1/2}$, $C_1 = C_2 = 960^{1/2} C_b/7(1 + C_b) S_k$, $C_e = (8\pi/27)^{1/3} C_S^{4/3}$, and $S_k = 0.5$. The SFS TKE is obtained from the same equation as the 1.5-order TKE closure. All NBA model parameters depend upon the backscatter coefficient, $C_b = 0.36$, and are formulated such that proper normal stresses are obtained for sheared homogeneous turbulence. In the limit $C_b \to 0$, the NBA1 and NBA2 models revert to the SMAG and TKE models, respectively (with different values for the constants).

e. Dynamic reconstruction model (DRM)

The DRM (Chow et al. 2005) is a mixed model, utilizing both an eddy-viscosity and a scale-similarity term. The eddy viscosity term is obtained following the scale-invariant dynamic formulation of Wong and Lilly (1994). The scale-similarity term is computed using explicit filtering and reconstruction of the resolvable subfilter-scale (RSFS) stresses. These are obtained by first reconstructing the ''unfiltered'' velocities, accomplished by applying the inverse of the explicit spatial filter to the (filtered) prognostic velocities. A series approximation is used for the inverse filter operation, for which the number of terms retained in the series determines the order of reconstruction. Next, Eq. (2) is used to compute the RSFS stresses by substituting the unfiltered velocities into u_i and u_j, and using one forward application of the explicit spatial filter (denoted by the tilde). Zero-order reconstruction (DRM0) uses the prognostic velocities themselves in Eq. (2) to compute the RSFS stresses. The DRM is stabilized using two (forward) applications of the explicit spatial filter.

For the DRM scalar fluxes, the eddy viscosity component is computed from Eq. (A3) using $K_q = P_r^{-1} K_M$ with $P_r^{-1} = 3$. The scale similarity component is computed analogously to the stresses (see Chow 2004 for details).

f. Near wall stress augmentation for dynamic models

The dynamic models (when implemented into WRF) require additional stresses near the surface due to underpredictions arising from coarse resolution. Following Brown et al. (2001), we use

$$\tau_{i3}^{w} = -\int_0^h c_w a(z) |\tilde{U}| \tilde{u}_i \, dz \,, \tag{A7}$$

where h_w is the height to which Eq. (A7) is applied, c_w is a scaling factor, and $a(z)$ is a shape function. Following Mirocha et al. (2013), we use $a(z) = e^{-(z/0.18h_w)^{\gamma}}$ and $h_w = 4\Delta x$ in each model. The LASD model uses $\gamma = 2$ and c_w values of 0.90 and 0.80 on the coarse and fine LES domains, respectively. The DRM uses $\gamma = 1$, and c_w values of 0.90 and 0.76 on the coarse and fine LES domains, respectively.

REFERENCES

Arya, S. P., 2001: *Introduction to Micrometeorology.* 2nd ed. Academic Press, 420 pp.

Bou-Zeid, E., C. Meneveau, and M. B. Parlange, 2005: A scale-dependent Lagrangian dynamic model for large eddy simulation of complex turbulent flows. *Phys. Fluids,* **17,** 025105, doi:10.1063/1.1839152.

——, N. Vercauteren, M. B. Parlange, and C. Meneveau, 2008: Scale dependence of subgrid-scale model coefficients: An a priori study. *Phys. Fluids,* **20,** 115106, doi:10.1063/1.2992192.

Brown, A. R., J. M. Hobson, and N. Wood, 2001: Large-eddy simulation of neutral turbulent flow over rough sinusoidal ridges. *Bound.-Layer Meteor.,* **98,** 411–441.

Caldwell, P., H.-N. S. Chin, D. C. Bader, and G. Bala, 2009: Evaluation of a WRF dynamical downscaling simulation over California. *Climatic Change,* **95,** 499–521.

Chow, F. K., 2004: Subfilter-scale turbulence modeling for large eddy simulation of the atmospheric boundary layer over complex terrain. Ph.D. dissertation, Stanford University, 339 pp.

——, R. L. Street, M. Xue, and J. H. Ferziger, 2005: Explicit filtering and reconstruction turbulence modeling for large-eddy simulation of neutral boundary layer flow. *J. Atmos. Sci.,* **62,** 2058–2077.

Deardorff, J. W., 1972: Numerical investigation of neutral and unstable planetary boundary layers. *J. Atmos. Sci.,* **29,** 91–115.

Holton, J. R., 1992: *An Introduction to Dynamic Meteorology*. 3rd ed. Academic Press, 511 pp.

Keating, A., U. Piomelli, E. Balaras, and H.-J. Kaltenbach, 2004: A priori and a posteriori tests of inflow conditions for large-eddy simulation. *Phys. Fluids,* **16,** 4696–4712.

Kirkil, G., J. D. Mirocha, F. K. Chow, and E. Bou-Zeid, 2012: Implementation and evaluation of dynamic subfilter-scale stress models for large-eddy simulation using WRF. *Mon. Wea. Rev.,* **140,** 266–284.

Kosović, B., 1997: Subgrid-scale modeling for the large-eddy simulation of high-Reynolds-number boundary layers. *J. Fluid Mech.,* **336,** 151–182.

Lilly, D. K., 1967: The representation of small-scale turbulence in numerical experiment. *Proc. IBM Scientific Computing Symp. on Environmental Sciences,* White Plains, NY, IBM, 195–210.

Liu, Y., and Coauthors, 2011: Simultaneous nested modeling from the synoptic scale to the LES scale for wind energy applications. *J. Wind Eng. Ind. Aerodyn.,* **99,** 308–319.

Lund, T., X. Wu, and D. Squires, 1998: Generation of turbulent inflow data for spatially developing boundary layer simulation. *J. Comput. Phys.,* **140,** 233–258.

Mirocha, J. D., J. K. Lundquist, and B. Kosović, 2010: Implementation of a nonlinear subfilter turbulence stress model for large-eddy simulation in the Advanced Research WRF model. *Mon. Wea. Rev.,* **138,** 4212–4228.

——, G. Kirkil, E. Bou-Zeid, F. K. Chow, and B. Kosović, 2013: Transition and equilibration of neutral atmospheric boundary layer flow in one-way nested large eddy simulations using the Weather Research and Forecasting Model. *Mon. Wea. Rev.,* **141,** 918–940.

Moeng, C.-H., J. Dudhia, J. B. Klemp, and P. P. Sullivan, 2007: Examining two-way nesting for large eddy simulation of the PBL using the WRF model. *Mon. Wea. Rev.,* **135,** 2295–2311.

Muñoz-Esparza, D., B. Cañadillas, T. Neumann, and J. van Beeck, 2012: Turbulent fluxes, stability and shear in the offshore environment: Mesoscale modelling and field observations at FINO1. *J. Renewable Sustainable Energy,* **4,** 063136, doi:10.1063/1.4769201.

Nakanishi, M., and H. Niino, 2004: An improved Mellor–Yamada level-3 model with condensation physics: Its design and verification. *Bound.-Layer Meteor.,* **112,** 1–31.

Piomelli, U., S. Kang, F. Ham, and G. Iaccarino, 2006: Effect of discontinuous filter width in large-eddy simulations of plane channel flow. *Studying Turbulence Using Numerical Simulation Database—XI, Proceedings of the Summer Program 2006,*

Center for Turbulence Research, 151–162. [Available online at http://ctr.stanford.edu/ctrsp06/piomelli.pdf.]

Skamarock, W. C., 2004: Evaluating mesoscale NWP models using kinetic energy spectra. *Mon. Wea. Rev.,* **132,** 3019–3032.

——, and Coauthors, 2008: A description of the advanced research WRF version 3. NCARTech. Note NCAR/TN-4751-STR, National Center for Atmospheric Research, 88 pp.

Smagorinsky, J., 1963: General circulation experiments with the primitive equations. *Mon. Wea. Rev.,* **91,** 99–152.

Thomas, T. G., and J. J. R. Williams, 1999: Simulation of skewed turbulent flow past a surface mounted cube. *J. Wind Eng. Ind. Aerodyn.,* **81,** 347–360.

Vanella, M., U. Piomelli, and E. Balaras, 2008: Effect of grid discontinuities on large-eddy simulation statistics and flow fields. *J. Turbul.,* **9,** 1–23.

Wong, V. C., and D. K. Lilly, 1994: A comparison of two dynamic subgrid closure methods for turbulent thermal-convection. *Phys. Fluids,* **6,** 1016–1023.

Wyngaard, J. C., 2004: Toward numerical modeling in the ''Terra Incognita.'' *J. Atmos. Sci.,* **61,** 1816–1826.

Zajaczkowski, F. J., S. E. Haupt, and K. J. Schmehl, 2011: A preliminary study of assimilating numerical weather prediction data into computational fluid dynamics models for wind prediction. *J. Wind Eng. Ind. Aerodyn.,* **99,** 320–329, doi:10.1016/j.jweia.2011.01.023.